

# 1 Detection of Extrasolar Planets by Gravitational Microlensing

David P. Bennett  
University of Notre Dame

No Institute Given

**Summary.** Gravitational microlensing provides a unique window on the properties and prevalence of extrasolar planetary systems because of its ability to find low-mass planets at separations of a few AU. The early evidence from microlensing indicates that the most common type of exoplanet yet detected are the so-called super-Earth planets of  $\sim 10$  Earth-masses at a separation of a few AU from their host stars. The detection of two such planets indicates that roughly one third of stars have such planets in the separation range 1.5-4 AU, which is about an order of magnitude larger than the prevalence of gas-giant planets at these separations. We review the basic physics of the microlensing method, and show why this method allows the detection of Earth-mass planets at separations of 2-3 AU with ground-based observations. We explore the conditions that allow the detection of the planetary host stars and allow measurement of planetary orbital parameters. Finally, we show that a low-cost, space-based microlensing survey can provide a comprehensive statistical census of extrasolar planetary systems with sensitivity down to 0.1 Earth-masses at separations ranging from 0.5 AU to infinity.

## 1.1 Introduction

The gravitational microlensing method relies upon chances alignments between background source stars and foreground stars, which may host planet systems. These background source stars serve as sources of light that are used to probe the gravitational field of the foreground stars and any planets that they might host. The relative motion of the source star and lens system allows the light rays from the source to sample different paths through the gravitational field of the foreground system, and it is changing total gravitational lens magnification of the source star with time that provides the observable gravitational microlensing signal.

The microlensing method is unique among exoplanet detection methods in a number of respects:

1. The amplitude of planetary microlensing signals is large (typically  $\gtrsim 10\%$ ) and is approximately independent of the planetary mass. Instead, the source-lens alignment necessary to give a detectable planetary signal depends on the planet-star mass ratio,  $q$ , and so the probability of a detectable planetary signal scales as  $\sim q$ .
2. This scaling of the probability of planet detection with the mass ratio,  $q$ , is shallower than the sensitivity curves for other methods, so microlensing is more sensitive to low-mass planets than other methods that are sensitive to planetary

mass. The sensitivity of the microlensing planet search method extends down to  $0.1M_{\oplus}$ .

3. Microlensing is most sensitive to planets at orbital separations of 1.5-4 AU, which corresponds to the vicinity of the Einstein ring radius. This range of separations also corresponds to the “snow line” where planet formation is most efficient according to the leading core accretion model of planet formation. Thus, microlensing complements the Doppler radial velocity and transit methods, which are most sensitive to planets in very short period orbits.
4. Microlensing is the only planet detection method that is sensitive to old, free-floating planets, which have been ejected from the gravitational potential well of their parent stars through planet-planet scattering. Theory predicts that such planets may be quite common, and ground-based microlensing can detect free-floating gas giant planets, while a space-based survey is needed to detect free-floating terrestrial planets.
5. Since the microlensing method doesn’t rely upon light from the host star in order to detect its planets, it can detect planets orbiting unseen stars. This can make it difficult to determine the properties of the host stars, but space-based follow-up observations can detect the host stars for most planets discovered by microlensing.
6. A space-based microlensing survey would provide a nearly complete statistical census of extrasolar planets with masses down to  $0.1M_{\oplus}$  at all separations  $\geq 0.5$  AU. This includes analogs of all the Solar System’s planets, except for Mercury.

Gravitational microlensing differs from other extrasolar planet search techniques in a number of aspects. It is a purely gravitational method that doesn’t rely upon on detecting photons from either the planet or its host star

While most of the known exoplanets have been discovered with the Doppler radial velocity method, the early results from the microlensing method indicate that cool, super-Earth or sub-Neptune mass planets are more representative of typical extrasolar planets than any of the 200+ exoplanets discovered by radial velocities.

## 1.2 Gravitational Microlensing Theory

### 1.2.1 The Single Lens Case

The basic physics of gravitational lensing depends only a single input from General Relativity, the deflection angle,  $\alpha$ , for a light ray passing a mass,  $M$ , with an impact parameter,  $r$ :

$$\alpha = \frac{4GM}{c^2 r} . \quad (1.1)$$

With the lens geometry shown in Fig. 1.1, we have

$$\alpha_i = \frac{4GM}{c^2(r_i - b)} = \frac{r_i D_S}{D_L(D_S - D_L)} , \quad (1.2)$$

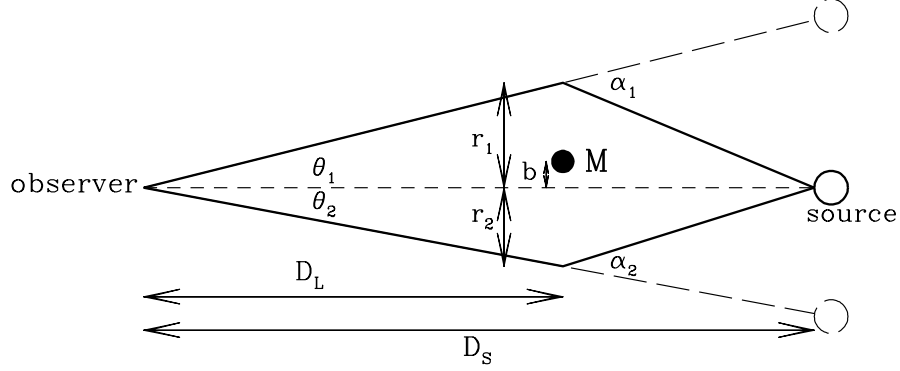


**Fig. 1.1.** The geometry of gravitational lens of mass,  $M$ , that is offset by a distance,  $b$ , from the line of sight to the source. The observer sees two images that are offset by angles,  $\theta_1$  and  $\theta_2$  from the line of sight to the source star.

in the small angle approximation. If the lens and source are perfectly aligned, the two images merge to form a ring of radius

$$R_E \equiv \theta_E D_L \equiv \sqrt{\frac{4GM D_L (D_S - D_L)}{c^2 D_S}}, \quad (1.3)$$

known as the Einstein ring radius. ( $\theta_E$  is the angular Einstein radius.) We can now rewrite the single lens equation as

$$r_i = \frac{R_E^2}{r_i - b}, \quad (1.4)$$

and it has two solutions:  $r_{+,-} = 0.5(b \pm \sqrt{b^2 + 4R_E^2})$ . The lensed images are also magnified, and the magnification of a source of infinitesimal size can be computed using area elements obtained by differentiating eq. 1.4. This yields

$$A_{+,-} = \frac{1}{2} \left( \frac{u^2 + 2}{u\sqrt{u^2 + 4}} \pm 1 \right), \quad (1.5)$$

where  $u \equiv b/R_E$  is the dimensionless lens-source separation. The total magnification of both images is given by

$$A = A_+ + A_- = \frac{u^2 + 2}{u\sqrt{u^2 + 4}}. \quad (1.6)$$

For a lens of  $M = 1M_\odot$ , that is half-way to a source in the Galactic center (at  $D_S = 8 \text{ kpc}$ ), we find

$$R_E = 4.04 \text{ AU} \sqrt{\frac{M}{M_\odot} \frac{D_S}{8 \text{ kpc}} 4x(1-x)}, \quad (1.7)$$

where  $x = D_L/D_S$ , so  $R_E$  is similar to the orbital radius of planets in our own Solar System. This also implies that  $\theta_E \sim 1$  mas. Since the image separation is of order  $\sim \theta_E$ , this implies that images will not generally be resolved with virtually all planned and future astronomical instruments (with a few exceptions (Delplancke et al., 2001)). On the other hand, if we assume a typical Galactic velocity of  $v_\perp = 100$  km/sec for the relative velocity between the lens star and the line-of-sight to the source, then the typical Einstein radius crossing time for a lens in the Galactic disk and a bulge source is  $t_E = R_E/v_\perp \sim 2$  months. Thus, the main observational effect for lensing by stars within the Milky Way is the time varying magnification instead of the image separation, and this is why it is referred to as microlensing instead of lensing.

The microlensing light curve is generally described by eq. 1.6 with the lens-source separation given by

$$u = \sqrt{\left(\frac{t - t_0}{t_E}\right)^2 + u_0^2}, \quad (1.8)$$

assuming that the relative motion between the lens and the observer-source line-of-sight. Thus, a single-lens microlensing light curve is described by three parameters, the time of peak magnification,  $t_0$ , the Einstein radius crossing time or width,  $t_E$ , and the minimum separation,  $u_0$ , which determines the peak magnification.  $u_0$  is the only parameter that affects the intrinsic light curve shape, as shown in Fig. 1.2, but only  $t_E$  constraints the physically interesting parameters of the event: the lens mass,  $M$ , the lens distance,  $D_L$ , and the relative velocity,  $v_\perp$ .

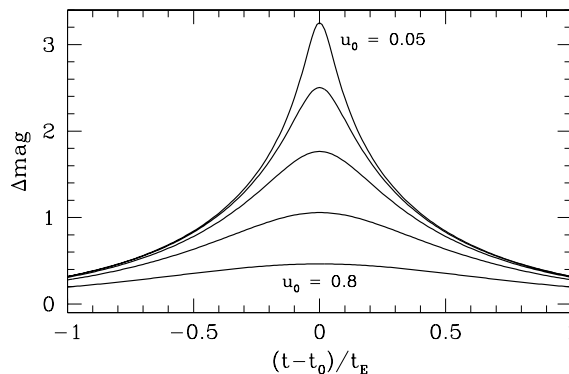


**Fig. 1.2.** Example microlensing light curves for a point source and a single lens that moves with a constant lens velocity with respect to the observer-source line-of-sight. Light curves with  $u_0 = 0.05, 0.1, 0.2, 0.4$ , and  $0.8$  are shown.

The first microlensing events were discovered in 1993 towards the Large Magellanic Cloud (LMC) by the MACHO Project (Alcock et al., 1993) and towards the Galactic bulge by the OGLE Collaboration. (Udalski et al., 1993). The early emphasis of microlensing surveys was the search for dark matter in the Milky Way's halo

(Paczynski, 1986), but this issue has been largely resolved with the demonstration that the excess microlensing seen toward the LMC by the MACHO group (Alcock et al., 2000b; Bennett, 2005) requires at most 20% of the Milky Way’s dark matter in the form of stellar mass objects, while the results of the EROS group (Tisserand et al., 2007) suggest that much of this microlensing excess may be caused by stars associated with the LMC itself (Sahu, 1994), perhaps in the LMC halo (Wu, 1994).

With the dark matter microlensing question mostly resolved, the prime focus of microlensing observations has shifted to the detection of extrasolar planets. Microlensing was first suggested as a method to find planets by Liebes (1964), but as Mao & Paczynski (1991) pointed out, this requires a consideration of multiple lens systems.

### 1.2.2 Multiple Lens Systems

The lens equation for a multiple lens system is a straight forward generalization of the single lens equation, eq. 1.4, but with more than one lens mass, we can no longer assume that the source, observer and lens system all lie in a single plane. However, as long as the distances to the lens and source ( $D_L$  and  $D_S$ ) are much larger than the extent of the lens system, we can assume that the lens system resides a single distance, and define the Einstein radius of the total lens system mass using eq. 1.3. So, as before, we will rescale all the length variables with  $R_E$ .

Because we can no longer define a source-lens-observer plane, we must now define the lens and source positions in the 2-dimensional “lens-plane” perpendicular to the line-of-sight and projected to the distance of the lens (or equivalently, we can just use angular variables for the positions of the source and lenses on the sky). The double-lens system was first solved using two real coordinates for the lens plane (Schneider & Weiss, 1986), but the algebra is much simpler if we describe the lens plane with complex coordinates following Bourassa et al. (1973); Witt (1990) and Rhie (1997). The generalization of eq. 1.4 is

$$w = z - \sum_i \frac{\epsilon_i}{\bar{z} - \bar{x}_i} , \quad (1.9)$$

where  $w$  and  $z$  are the complex positions of the source and image, respectively, and  $x_i$  are the complex positions of the lens masses. The individual lens masses are represented by  $\epsilon_i$ , which is the mass fraction of the  $i$ th lens mass, so that  $\sum_i \epsilon_i = 1$ . The appearance of the complex conjugates in the denominator in the sum on the right side of eq. 1.9 is simply a reflection of the fact that the lens deflection is in the direction from the source to the lens with a magnitude of the inverse of that distance. With real coordinates, we would express this as the vector difference of the positions divided by this vector squared, but with complex coordinates, we can divide through by this vector leaving only its complex conjugate in the denominator.

If we knew the position of the images,  $z$ , in eq. 1.9, then it would be trivial to solve for the position of the source. But this is the inverse of the problem that we will usually want to solve, which is to find the positions of the images based on

a known position for the source. However, the solution of this “inverse” problem is the basis of the brute-force, ray-shooting method (Schneider & Weiss, 1987) for solving eq. 1.9. This method involves taking a large grid of points in the “image plane” and propagating them back to the source plane using eq. 1.9. This method has the advantage that it can handle very complicated lens mass distributions, but it is usually not the method of choice for the analysis of microlensing events.

The most successful method for calculating multi-lens microlensing light curves (Bennett & Rhie, 1996) involves solving eq. 1.9 for the positions of the point-source images and invoking the ray-shooting method only in the vicinity of images that are affected by finite-source size effects. For the majority of the light curve, the finite-source calculations are not needed, and we can use the point source magnification formula. This formula can be derived from the Jacobian determinant of the lens equation (and its complex conjugate):

$$J = \frac{\partial w}{\partial z} \frac{\partial \bar{w}}{\partial \bar{z}} - \frac{\partial w}{\partial \bar{z}} \frac{\partial \bar{w}}{\partial z} = 1 - \left| \frac{\partial w}{\partial \bar{z}} \right|^2, \quad (1.10)$$

where

$$\frac{\partial w}{\partial \bar{z}} = \sum_i \frac{\epsilon_i}{(\bar{z} - \bar{x}_i)^2}. \quad (1.11)$$

Because eq. 1.10 gives the Jacobian determinant of the inverse mapping from the image plane to the source plane, the magnification of each image is given by

$$A = \frac{1}{|J|}, \quad (1.12)$$

evaluated at the position of each image.

The solution of the lens equation, 1.9, is non-trivial. For the case of two lens masses, this equation can be embedded into a fifth order polynomial equation in  $z$ , which can be solved numerically. This equation has either 3 or 5 solutions (Witt, 1990; Rhie, 1997) that correspond to solutions of 1.9, which means that a double lens system must have either 3 or 5 images depending on the configuration of the lens system and the location of the source. For the triple lens case (which is relevant for at least one planetary microlensing event), the lens equation can be embedded in a rather complicated tenth order polynomial that has 4, 6, 8, or 10 solutions that correspond to physical images (Rhie, 2002). This tenth order polynomial equation can be solved numerically, although it may require extended precision numerical calculations in order to avoid serious round-off errors (Bennett et al., in preparation). The case of 4 lens masses, has also been investigated (Rhie, 2001), but the lens equation has not been converted to a polynomial.

The most important feature of lensing by multiple masses occurs at the locations where  $J = 0$ . From eq. 1.12, this implies infinite magnification for a point source. (The magnification is always finite for the realistic case of a source of finite angular size.) For a single lens,  $J = 0$  only occurs at a single point in the source plane, the location of the lens mass, but for lens systems with more than one mass, there are a set of one or more closed curves with  $J = 0$ , known as critical curves. The

source positions corresponding to the critical curves are obtained by applying the lens equation, 1.9, and they are referred to as caustic curves. When the source passes to the interior of a caustic curve, two new images are created, and it is these new images that have infinite magnification for the (unphysical) case of a point source. The shape of the light curve of a (point) source crossing a caustic has a characteristic form:

$$A = \frac{F_c \Theta(x - x_c)}{\sqrt{x - x_c}} + A_{nc} , \quad (1.13)$$

where  $F_c$  gives the amplitude of the caustic,  $A_{nc}$  gives the magnification of the images that are not associated with the caustic and  $\Theta(x) = 1$  for  $x \geq 0$  and  $\Theta(x) = 0$  otherwise.  $x$  is the distance perpendicular to the direction of the caustic curve, and  $x_c$  is the location of the caustic curve. Eq. 1.13 is a good approximation to the magnification for a point source when the curvature of the caustic curve can be neglected. Note, that the singularity in eq. 1.13 is weak enough so that the integral of this formula will yield a finite magnification for a finite size source star.

Caustic crossings that follow the form of eq. 1.13 are often referred to as *fold* caustic crossings, and they have the feature that there is essentially no warning that the caustic crossing is imminent when the caustic curve is approached from the outside (*i.e.*  $x < x_c$ ). This is because the magnification pattern for a fold caustic extends only to the interior of the caustic since it involves the magnification of images that only exist inside the caustic curve. However, each caustic curve also has at least three sharp pointy features, known as cusps, and the magnification pattern extends outward from the cusps on a caustic curve. The magnification scales as the inverse of the distance to the cusp, just as in the single lens case, eq. 1.6.

The path of the source with respect to the caustic curves provides the basic characteristics of a multiple lens microlensing light curve. Multiple lens light curves frequently have features which match the expected  $A \sim \Theta(x)x^{-1/2}$  shape of a caustic crossing or the  $A \sim r^{-1}$  shape of a cusp approach. But, there are additional complications, as the strength of a caustic crossing ( $F_c$  in eq. 1.13) can vary and the angular size of the source star can sometimes be larger than the entire caustic curve for a planetary microlensing event.

### 1.3 Planetary Microlensing Events

Planetary microlensing events are a subset of multiple lens events where the mass ratio is quite small. Planetary events have light curves that appear quite similar to the single lens light curves shown in Fig. 1.2, but for a brief period of time they deviate from the single lens form and display the characteristics of a binary lens light curve. We will define a requirement on the mass ratio  $q \equiv \epsilon_2/\epsilon_1 < 0.03$  to separate planetary microlensing events from stellar binary events following Bond et al. (2004), because  $q \approx 0.03$  is the approximate location of the “brown dwarf desert” that appears to separate stellar from planetary secondaries. We will also initially only consider events with only one detectable planet, as these represent the majority of planetary microlensing events and this will simplify the discussion.

The caustic structure of a binary lens system is determined by the mass ratio and the separation of the lenses (Schneider & Weiss, 1986). For a separation  $d \ll 1$  (in units of  $R_E$ ), there are three caustics, two triangular caustics with 3 cusps each and a caustic close to the center of mass which has 4 cusps. These merge into a single caustic with 5 cusps at  $d \sim 1$ , which splits into two caustic curves with 4 cusps each for  $d \gg 1$ . For small values of the mass ratio,  $q$ , the division between these regimes occurs near  $d \approx 1$ , so most events have multiple caustic curves. As shown in Fig. 1.3.

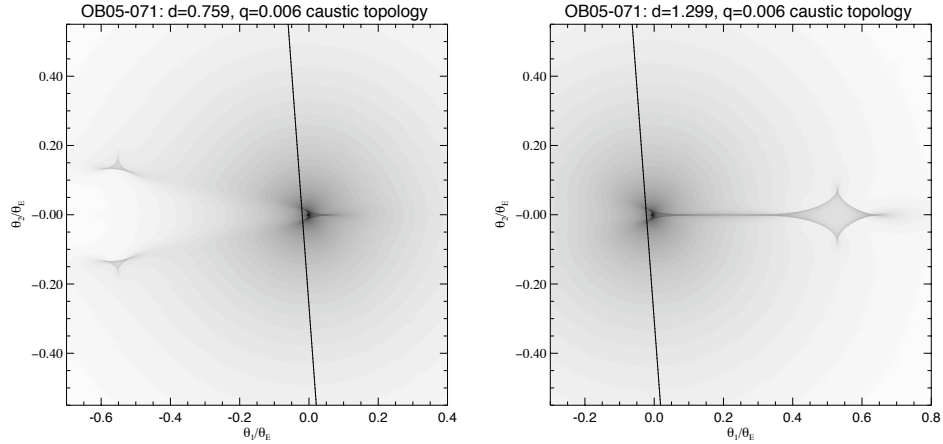


**Fig. 1.3.** Grey-scale magnification patterns for two models of the planetary microlensing event OGLE-2005-BLG-71. The darkness of the image is proportional to the logarithm of the magnification. The nearly vertical lines in each panel indicate the path of the source star for each model. The source passes close to the central, or stellar, caustic, and as discussed in § 1.4, the magnification pattern in the vicinity of the central caustic is similar for planetary systems related by  $d \leftrightarrow 1/d$ . The magnification patterns for the planetary caustics (on the outside of each panel) are clearly very different and easy to distinguish. (These images are provide courtesy of Daniel Kubas.)

### 1.3.1 Planetary Caustic Perturbations

There are two classes of caustic curves in planetary microlensing events: planetary caustics and the stellar or central caustic. The planetary caustics result when one of the two light rays in Fig. 1.1 passes close to the planet and is deflected by the planetary gravitational field of the planet. The locations of the caustics are given by

$$s_c = d - 1/d . \quad (1.14)$$

If we see a planetary deviation at a point where the best fit single lens light curve predicts a magnification,  $A$ , we can find the corresponding  $u$  value by inverting



eq. 1.6 to get  $u_c = s_c$ , and then solve for  $d$  by inverting eq. 1.14 to give

$$d = \frac{1}{2} \left( u_c \pm \sqrt{u_c^2 + 4} \right) . \quad (1.15)$$

The two solutions to eq. 1.15 for a given  $u_c$  value are referred to as major and minor image perturbations. They were first studied in detail by Gould & Loeb (1992) who showed that many features of the planetary caustics and their magnification pattern could be explained by the simpler Chang-Refsdal lens system (Chang & Refsdal, 1979, 1984). Several important features of the planetary caustic light curve perturbations can be seen in Fig. 1.3. The left side of the left panel of this figure shows the magnification pattern of the two roughly triangular minor image caustic, which are generated by a planet with  $d < 1$ . As with all caustics, there is excess magnification in the interior of the caustic curve, as well as extending outward from the cusps. But there is also a very pronounced magnification deficit in between the two minor image caustics, where the magnification is substantially below the single lens magnification. In contrast, the magnification pattern for the major image caustic (shown on the right side of the right panel in Fig. 1.3) is predominantly positive, with only small magnification deficits very close to the caustic curve, away from the 4 cusps.

### 1.3.2 Stellar Caustic Perturbations

It was originally suspected that the planetary caustic perturbations would be the best way to detect planetary signals in microlensing events, but Griest & Safizadeh (1998) argued that there were a number of advantages to searching for planetary light curve perturbations due to the stellar caustic. They showed that the planet detection efficiency for each high magnification event was substantially higher than for events of more modest magnification. While the higher planet detection efficiency for higher magnification events was seen in previous work (Bolatto & Falco, 1994; Bennett & Rhie, 1996), Griest & Safizadeh (1998) emphasized that this effect is quite dramatic and that this fact could be used to increase the observational planet detection efficiency. In the same year that the Griest & Safizadeh paper was published, the MPS and MOA Collaborations demonstrated this method with observations of the MACHO-98-BLG-35 event. The subsequent analysis showed (Rhie et al., 2000) that the lens star for this event did not have any Jupiter-mass planets with a projected separation of 0.6-8 AU.

The high planet detection efficiency for high magnification events is particularly useful when a large number of microlensing events are discovered by the microlensing survey groups. This is the current situation, as the OGLE-3 and MOA-2 surveys combine to detect  $> 700$  microlensing events in progress toward the central regions of the Milky Way between February and October of each year. Relatively sparse monitoring of events (*i.e.* one or two observations per day) is required to predict most high magnification events in advance, and this allows observing resources can be focused on events with a high planet detection efficiency.

One important consequence of the high planet detection efficiency for high magnification events is that the chances of detecting multiple planets in such events are greatly enhanced (Gaudi et al., 1998). Indeed, the first multi-planet system discovered by microlensing is shown below in § 1.5.2. There is, however, a potential downside to this higher sensitivity to multiple lens masses. The signals for all the detectable lens masses will be concentrated in the very high magnification part of the light curve, and this could make it difficult to work out the details of multiple planet systems that are detected in microlensing events. Thus, the development of efficient light curve modeling methods for lens systems with three or more masses is an important active area of current research.

A final advantage of high magnification events is that they allow planet detection with relatively faint source stars. This makes it much easier to detect the planetary host star with follow-up observations (Bennett et al., 2007a) as explained in § 1.4.1.

### 1.3.3 Finite Source Effects

Microlensing is arguably the exoplanet search technique that is most sensitive to low-mass planets, and lower limit in sensitivity of the microlensing method is set by the finite angular size of the source stars. Roughly speaking, when the angular radius of the planetary Einstein ring,  $\sqrt{\epsilon_p}\theta_E$ , is much smaller than the source star angular radius,  $\theta_*$ , we expect that planetary signal to be washed out. But this is only a crude, order-of-magnitude estimate, and a full finite source solution to the lens equation, 1.9, is required to determine the precise limits on the microlensing planet detection method set by the finite angular size of the sources.

Full finite source planetary microlensing light curves were first calculated by Bennett & Rhie (1996) using the methods described in § 1.2.2. Results of these calculations are reproduced in Figs. 1.4 and 1.5. Fig. 1.4 shows a series of planetary light curves with planetary mass fractions of  $\epsilon = 10^{-4}$  and  $10^{-5}$ . For a typical lens star mass of  $\sim 0.3M_\odot$ , these correspond to  $1M_\oplus$  and  $10M_\oplus$ , respectively. The finite source light curves are characterized by the source star radius in Einstein ring units:  $\rho \equiv \theta_*/\theta_E$ . The  $\rho$  values shown in Fig. 1.4 are 0.003, 0.006, 0.013, and 0.03, and these span the expected range of  $\rho$  for a low mass planetary host star in the Galactic bulge with a source star ranging in radius from  $1R_\odot$  to  $10R_\odot$ , which is a typical radius for a “red clump” K-giant in the bulge. A number of the planet detections to date actually have  $\rho$  values in the  $0.4\text{--}1 \times 10^{-3}$  range because the lens stars reside in the bulge and have a larger than average mass. (Both of these imply a larger  $\theta_E$ .)

Several general trends are apparent from Fig. 1.4. First, the planetary deviations are easily detectable for  $\rho = 0.003$ , but the signals are much weaker for  $\rho = 0.03$ . This implies that  $1M_\oplus$  planets are easily detected with main sequence source stars, but planets of  $10M_\oplus$  are close to the lower limit of detectability for giant source stars. Another notable feature of these light curves is that the planetary signals with  $d = 0.8$  are more easily washed out by the finite source effects than those with  $d = 1.3$ . This is a consequence of the large magnification deficit seen between the two planetary caustics for a minor image perturbation, as shown in the left hand panel of Fig. 1.3. When a large finite source effectively averages over the vicinity of a minor

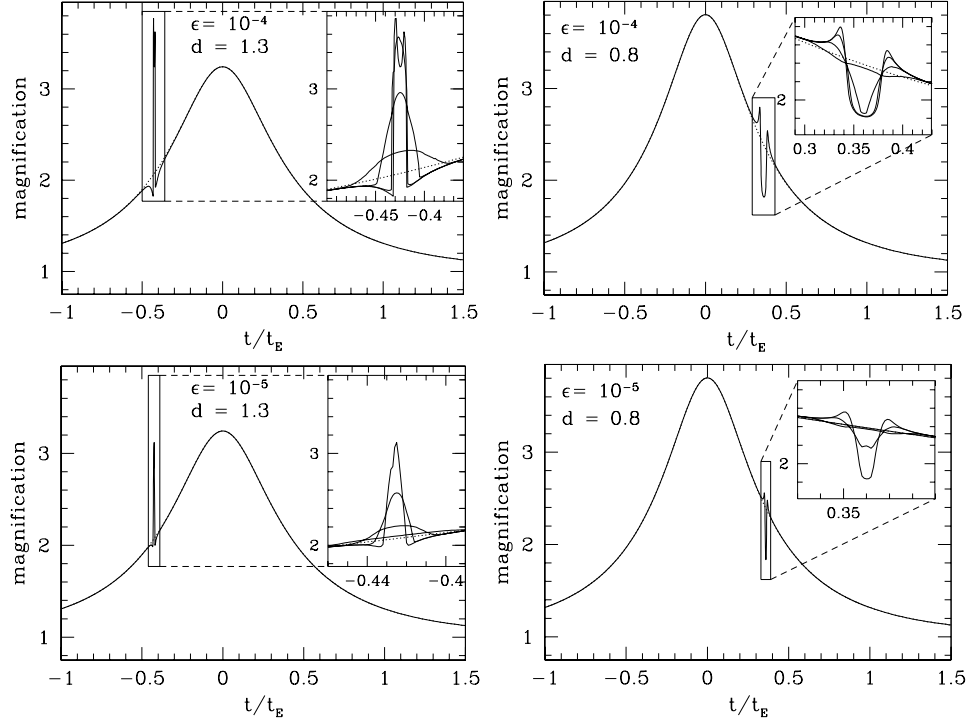


**Fig. 1.4.** Microlensing lightcurves which show planetary deviations are plotted for a mass ratio of  $\epsilon = 10^{-4}$  &  $10^{-5}$  and separations of  $d = 1.3$  &  $0.8$ . The main plots are for a stellar radius of  $\rho = 0.003$  while the insets show light curves for radii of  $0.006$ ,  $0.013$ , and  $0.03$  as well. The dashed curves are the unperturbed single lens lightcurves. For each of these lightcurves, the source trajectory is at an angle of  $\sin^{-1} 0.6$  with respect to the star-planet axis. The impact parameter  $u_0 = 0.27$  for the  $d = 0.8$  plots and  $u_0 = 0.32$  for the  $d = 1.3$  plots.

image planetary caustic, the positive and negative deviations effectively cancel each other out (Bennett & Rhie, 1996; Gould & Gaucherel, 1997). In contrast, the major image planetary caustic magnification deviation pattern is mostly positive, so the finite source effect merely smoothes it out.

Fig. 1.5 shows how the planet detection probability varies as a function of  $d$  for the same  $\epsilon$  and  $\rho$  values used for Fig. 1.4. The greater tolerance of deviations with  $d > 1$  to finite source effects is apparent for  $\epsilon = 10^{-4}$ ,  $\rho = 0.03$  and  $\epsilon = 10^{-5}$ ,  $\rho = 0.013$ . The behavior of Fig. 1.5 near  $d = 1$  is even more interesting. For  $\epsilon = 10^{-4}$  and  $\rho = 0.003$  or  $0.006$ , the detection probability reaches a maximum at  $d \approx 1$ , but for  $\rho = 0.013$ , the probability has a local minimum at  $d = 1$ , and for  $\rho = 0.03$  or any of the  $\rho$  values with  $\epsilon = 10^{-5}$ , the detection probability = 0 at  $d = 1$ . This is due to the fact that for  $d \approx 1$  the planetary and stellar caustics merge to form a relatively large single caustic that is extended along the lens axis. This caustic

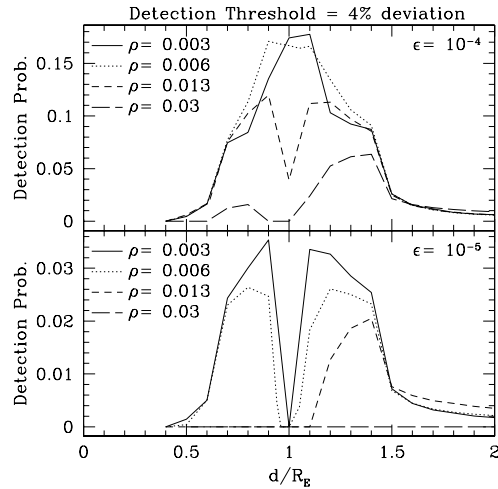


**Fig. 1.5.** The planetary deviation detection probability is plotted for different values of the planetary mass ratio,  $\epsilon$ , and the stellar radii,  $\rho$  (in units of  $R_E$ ). A planet is considered to be “detected” if the lightcurve deviates from the standard point lens lightcurve by more than 4% for a duration of more than  $t_E/200$ .

is large, but relatively weak, and it has associated positive and negative deviation regions that tend to cancel when averaged over by a moderately large finite source.

However, some features of Fig. 1.5 are dependent on the somewhat arbitrary choice of the event detection threshold, and the sensitivity of a real observing strategy can differ from this. In fact, the planetary deviation detected in event OGLE-2005-BLG-169 (Gould et al., 2006) would not have passed the selection criteria for Fig. 1.5, but the planet is nevertheless detected with a strong signal. The reason for this is that it was identified as a very high magnification event with a very high sensitivity to planets, and for this reason it was observed much more frequently than most events with potential planetary signals. The additional observations provided enough additional signal to allow the definitive detection of a relatively low-amplitude signal.

As a practical matter, finite source effects imply a lower planetary mass limit of  $M_p \gtrsim 5M_\oplus$  for giant source stars in the bulge, and a limit of  $M_p \gtrsim 0.05M_\oplus$  for bulge main sequence stars. Thus, searches for terrestrial exoplanets must focus on main sequence source stars.

## 1.4 Planetary Parameters from Microlensing Events

The determination of the properties of the lens systems that are detected in microlensing events is often a serious challenge. The simple form of the microlensing light curves shown in Fig. 1.2 is an advantage when trying to identify microlensing events, but as I mentioned in § 1.2.1, in a single lens event, it can also be a drawback

when trying to interpret observed microlensing events. For most single lens events, it is only the  $t_E$  parameter that constraints the physically interesting parameters of the event: the lens mass,  $M$ , the lens distance,  $D_L$ , and the relative velocity,  $v_\perp$ . The single lens parameters  $u_0$  and  $t_0$  don't constrain lens system parameters that are of much interest.

In addition to the parameters needed to describe a single lens event, a planetary microlensing event must have three additional binary lens parameters: the planetary mass ratio,  $q = \epsilon/(1-\epsilon)$ , the star-planet separation,  $d$ , (which is in units of  $R_E$ ), and the angle between the star-planet axis and the trajectory of the source with respect to the lens system,  $\theta$ . So, two of these new parameters,  $q$  and  $d$ , directly constrain planetary parameters of interest, although  $d$  is normalized to  $R_E$ , which may not be known. Most planetary light curves, at least those for low-mass planets, also have caustic crossings or a close approach to a cusp that reveal light curve features due to the finite size of the source star. This enables the source radius crossing time,  $t_*$ , to be measured.

The determination of the star-planet separation and the planetary mass fraction is usually quite straightforward from the microlensing light curve. For events at moderate magnification, due to the planetary caustic, the separation can be determined by the magnification predicted by the single lens model that describes the event outside the region of the planetary deviation following eq. 1.15. This still leaves an ambiguity between the  $d < 1$  and  $d > 1$  solutions, but this is easily resolved by the drastically different magnification patterns in the vicinity of major image and minor image caustics, as shown in Fig. 1.3. The planetary mass fraction,  $q$ , can generally be determined by the duration of the planetary perturbation. In some cases, if the time scale of the deviation is similar to or smaller than  $t_*$ , both  $q$  and  $t_*$  determine the deviation time scale, but good light curve coverage with moderately precise photometry allow both  $q$  and  $t_*$  to be determined (Gaudi & Gould, 1997).

The situation is somewhat different for high magnification, stellar caustic deviation events. Dominik (1999) pointed out an approximate degeneracy in the properties of the stellar caustic under the transformation  $d \rightarrow 1/d$ , which means that there may be a  $d \leftrightarrow 1/d$  ambiguity in the modeling of stellar caustic planetary events. This is apparent from the magnification patterns shown in Fig. 1.3. For as source trajectory nearly parallel to the lens axis or for  $d \sim 1$ , this degeneracy breaks down, so the ambiguity disappears. With precise photometry it is usually possible to distinguish between the  $d < 1$  and  $d > 1$  solutions, and this has been the case for all events observed to date.

#### 1.4.1 Angular Einstein Radius

A large fraction of planetary light curve deviations exhibit finite source effects that allow the source radius crossing time,  $t_*$ , to be measured. This is the case for most detectable events with a planetary mass,  $M_p \lesssim 10M_\oplus$ , but for gas giant planets of  $M_p \gtrsim 300M_\oplus$ , it is possible to detect a planetary deviation without the source

crossing a caustic or coming close enough to a cusp to display finite source effects. So,  $t_*$  is measurable for most, but not all planetary microlensing events.

When  $t_*$  is measured, it is possible to place an additional constraint, as long as the angular radius of the source star,  $\theta_*$ , can be estimated, because the angular Einstein radius is given by

$$\theta_E = \frac{\theta_* t_E}{t_*} . \quad (1.16)$$

The angular radius of the source star can be measured if the brightness and color of the source are known with the use of empirical color-angular radius relations (van Belle, 1999; Kervella et al., 2004). In the crowded fields where microlensing events are observed, the most reliable measure of the source star brightness and color comes from the light curve models, which include the source brightness as a model parameter. So, although it is sufficient to measure the detailed light curve shape in a single passband, it is important to obtain a few measurements during the microlensing event in at least one additional passband so that the light curve fit will also reveal the color of the source. It is also important to estimate the extinction towards the source. With measurements in only two colors, such as  $V$  and  $I$ , the extinction can be estimated by comparison to the red clump giant stars within an arc minute or two of the target star (Yoo et al., 2004). While this does not yield a precise measure of the extinction to the source, note that an error in the extinction to the source will affect both the estimated intrinsic brightness and color of the source. Fortunately, the extinction-induced brightness and color errors have the opposite effect on the estimated source star radius. This partial cancellation implies that the estimated  $\theta_*$  value is not very sensitive to the uncertainty in the extinction.

A more precise estimate of  $\theta_*$  can be obtained with observations during the microlensing event in more than two passbands, particularly if one of the passbands is in the infrared because the optical-IR color-radius relations are much more precise than the optical ones (Kervella et al., 2004) and because extinction is much lower in the IR than in the optical. Observations in 3 or more colors also allow an estimate of extinction that doesn't depend the nearby clump giants, with the use of empirical color-color relations (Bessell & Brett, 1998).

When the angular Einstein radius is measured, we have the following relation,

$$M_L = \frac{c^2}{4G} \theta_E^2 \frac{D_S D_L}{D_S - D_L} , \quad (1.17)$$

which can be considered to be a mass-distance relation because  $D_S$  is generally known (approximately) from the brightness and color of the source. (The high density of stars in the Galactic bulge means that the source is almost always a bulge star.) Eq. 1.17 provides a one-parameter family of solutions to the microlensing event, and this can be converted to a measurement of the planetary host star properties with one additional piece of information. Since the brightness of the source star can be determined by the light curve fit, the brightness of the lens star can be determined with an image that has sufficient angular resolution to resolve the source

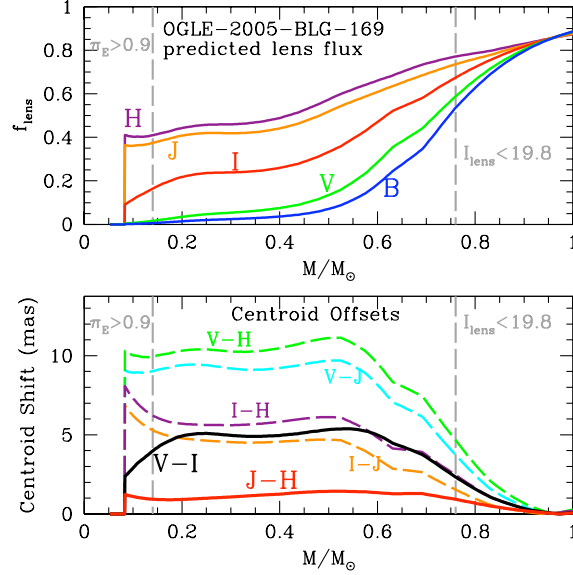


**Fig. 1.6.** The predicted fractional brightness,  $f_{\text{lens}} = F_L/(F_S + F_L)$ , of the OGLE-2003-BLG-169 lens is plotted in the top panel as a function of mass in the *BVIJH* passbands. ( $F_L$  and  $F_S$  and the detected flux of the lens and source, respectively). The predicted offsets of the centroids of the blended source+lens images in different passbands are shown in the bottom panel, assuming that the images are taken 2.4 years after peak magnification.

and lens stars from the unrelated stars in the field. This generally requires space-based imaging with the Hubble Space Telescope (HST), or possibly ground-based adaptive optics imaging because of the extreme crowding in the Galactic bulge fields where microlensing events are most easily found. (The lens-source relative proper motion has typical value  $\mu_{\text{rel}} \sim 5 \text{ mas/yr}$ , so the lens and source are not typically resolved from each other until a decade or more after the event.) If the combined lens-plus-source image is significantly brighter than the brightness of the source from the microlensing fit, then the difference determines the brightness of the lens. This then allows the mass of the planetary host (lens) star to be determined using a main sequence star mass-luminosity relation (Bennett et al., 2007a).

The top panel of Fig. 1.6 shows the predicted brightness of the lens for the OGLE-2005-BLG-169 event in the *BVIJH* passbands. This indicates that the lens star will easily be detected if it is a main sequence star, since even a  $0.08M_{\odot}$  lens star will contribute  $\gtrsim 40\%$  of the *H*-band flux and  $\gtrsim 10\%$  of the *I*-band flux. This case is more favorable than most because of a relatively large  $\theta_E$  value, but most cases, the lens star will be detectable in the *H*-band unless it is a late M-dwarf located in the bulge. However, for Galactic disk lenses at a certain range of distances (corresponding to  $0.2M_{\odot} \lesssim M \lesssim 0.4$  for OGLE-2005-BLG-169 in the *IJH*-bands) the mass-distance relation, eq. 1.17, combines with the mass-luminosity relation to

yield a nearly flat mass-brightness relation for the planetary host star. In these cases, it is useful to have images in shorter wavelength bands, such as  $V$  and  $B$  because this cancellation does generally not occur in the optical and infrared passbands for the same range of lens star masses.

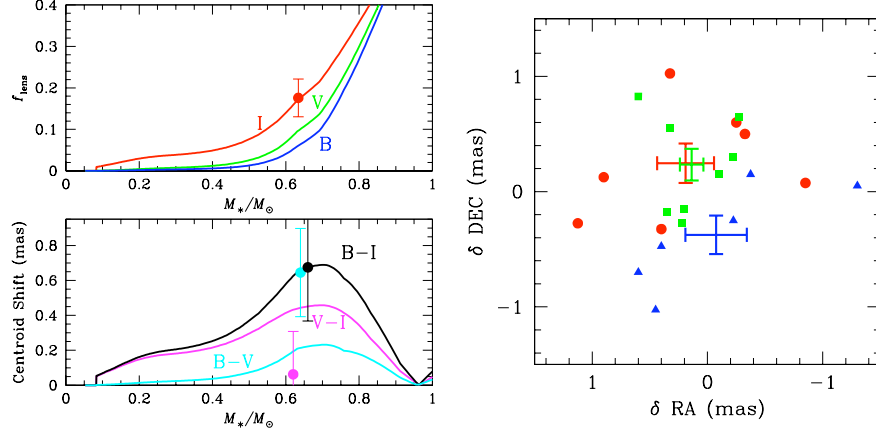


**Fig. 1.7.** The top-left panel shows the fraction of the source+ lens flux for event OGLE-2003-BLG-235/MOA-2003-BLG-53 that is predicted to come from the lens in the HST- $I$ ,  $V$ , and  $B$  passbands as a function of lens mass. The bottom-left panel shows the predicted color-dependent centroid shifts as a function of mass for 1.78 years of relative proper motion at  $\mu_{\text{rel}} = 3.3 \text{ mas/yr}$ . The measured values of  $f_{\text{lens}}$  in the  $I$ -band and the color dependent centroid shifts and error bars are indicated with their error bars. These are plotted at an arbitrary value for the stellar mass ( $M_*$ ). The centroids of the source+ lens star blended images in the individual HST/ACS/HRC images are shown in the right panel as red circles ( $I$ ), green squares ( $V$ ), and blue triangles ( $B$ ). The crossed error bars are the average centroid in each passband.

High resolution images in multiple colors also allow an independent method for estimating the lens star brightness, as shown in the bottom panel of Fig. 1.6 and the bottom-left panel of Fig. 1.7. Because the lens and source stars usually have different colors, the centroid of the blended source+ lens image will usually be color dependent. So, an additional constraint on the lens star is obtained by measuring the centroid offset between the centroids of the blended source+ lens in different passbands. As indicated in Fig. 1.7, this effect was marginally detected for the first planet detected by microlensing (Bennett et al., 2006) with HST images taken only 1.8 years after peak magnification. Also, because this color dependent centroid shift depends on the relative lens-source proper motion,  $\mu_{\text{rel}}$ , it can be used to help determine  $\theta_E$  for planetary events with no finite source effects, and hence, no measurement of  $t_*$ .

The stable point-spread function (PSF) of space-based telescopes, such as HST, allows the measurement of the image elongation due to the growing separation of



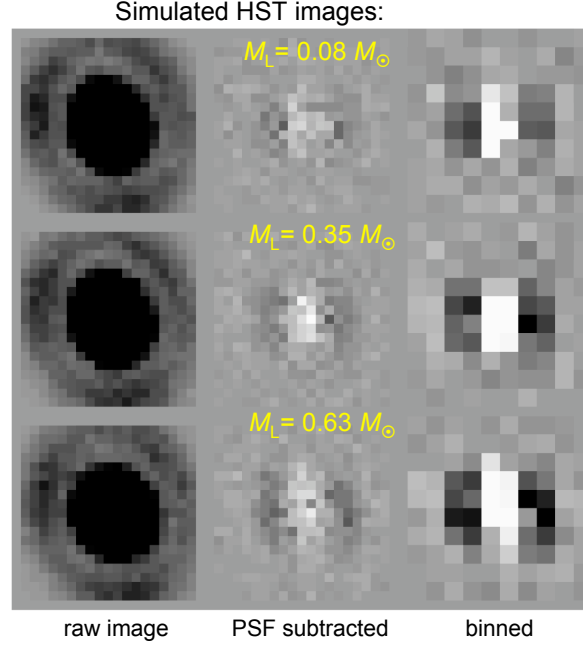


**Fig. 1.8.** Simulated image stacks of multiple dithered exposures of the OGLE-2005-BLG-169 source and lens star 2.4 years after peak magnification using the HST/ACS High Resolution Camera (HRC) in the F814W filter band. The top row of images assumed a host star mass of  $M_* = 0.08M_\odot$ , the middle row assumes  $M_* = 0.35M_\odot$ , and the bottom row assumes  $M_* = 0.63M_\odot$ . In each row, the image on the left shows the raw image stack sampled at one half the native HRC (28 mas) pixel size. The central column shows the residuals after subtraction of the best fit PSF model, showing the blended image elongation along the  $x$ -axis due to the lens-source separation. The right hand column shows these residuals rebinned to the 28 mas native pixel scale.

the lens and source stars after the microlensing event. Simulations of this effect for the OGLE-2005-BLG-169 event are shown in Fig. 1.8 for three different cases:  $M_L = 0.08M_\odot$ ,  $M_L = 0.35M_\odot$ , and  $M_L = 0.63M_\odot$ . This event has a higher relative proper motion than most events, but this simulation assume images taken only 2.4 years after peak magnification, so for other events, it may be necessary to obtain the follow-up space-based images  $\sim 4$  years after peak magnification.

When  $\mu_{\text{rel}}$  can be measured from image elongation and/or the color dependent centroid shift, then the angular Einstein radius can be determined via

$$\theta_E = \mu_{\text{rel}} t_E , \quad (1.18)$$

so that mass-distance relation can be determined even when  $t_*$  cannot be measured.

### 1.4.2 Microlensing Parallax

Another method to “solve” a microlensing event involves the microlensing parallax effect. This refers to measurements of  $\tilde{r}_e = R_E D_S / (D_S - D_L)$ , the Einstein radius projected to the position of the Solar System.  $\tilde{r}_e$  can be measured with the help of observations of microlensing events by observers at different locations. Because the Einstein radius is typically of order  $R_E \sim 1$  AU, the observers must generally be separated by a distance of  $\sim 1$  AU. The conceptually simplest way to do this is to observe an event simultaneously with a satellite in a heliocentric orbit, (Refsdal, 1966; Gould, 1992), as has recently been done with Spitzer (Dong et al., 2007). However, it is much more common to use the orbital motion of the Earth to measure the microlensing parallax effect (Alcock et al., 1995; Mao, 1999; Smith et al., 2002; Bennett et al., 2002; Mao et al., 2002), but for events of very high magnification, it is possible to measure this effect with observations from different observatories on Earth (Gould, 1997), as has recently been done by Gould et al. (2007, in preparation).

A potential complication with this method is that the orbital motion of the source star can mimic the effect of the orbital motion of the Earth, but if the signal is strong, it is generally possible to detect the characteristic features of the Earth’s orbit (Poindexter et al., 2005). Another potential complication is that for events with  $t_E \ll 1$  yr, it is often possible to measure only a single component of the two-dimensional  $\tilde{\mathbf{r}}_e$  vector (Smith et al., 2003). But, for events with detectable lens stars, the two-dimensional relative proper motion,  $\boldsymbol{\mu}_{\text{rel}}$ , it is possible to determine the full  $\tilde{\mathbf{r}}_e$  vector because  $\tilde{\mathbf{r}}_e \parallel \boldsymbol{\mu}_{\text{rel}}$ .

When  $\tilde{r}_e$  and  $\theta_E$  are both measured, the lens system mass is given by

$$M_L = \frac{c^2}{4G} \tilde{r}_e \theta_E . \quad (1.19)$$

This method has been used to determine the lens mass for a binary star lens system towards the Galactic bulge (An et al., 2002) and a low-mass M-dwarf lens towards the Large Magellanic Cloud (Gould, Bennett, & Alves, 2004). The first use of this method in a planetary microlensing event is the case of the double planet event OGLE-2006-BLG-109, to be published later this year (Gaudi et al. 2007, in preparation; Bennett et al. 2007, in preparation).

### 1.4.3 Planetary Orbits

The final property of a planetary system that can be measured is the orbital motion of the planet with respect to the star. This is a lower order effect than microlensing parallax because we see the effects of both the planet and the star in the light curve. So, we are sensitive to the relative velocity between the star and planet, whereas the velocity of the Earth around the Sun cannot be separated from the lens-source relative velocity. However, the time scale of the planetary deviation is generally only a small fraction of the microlensing light curve, and this limits the amount of time over which we can detect the orbital motion effects. Also, the typical orbital

period of a planet detected by microlensing is  $\sim 10$  yrs, so the orbital velocities are generally lower than that of the Earth around the Sun.

The for a planetary deviation of duration  $\Delta t$  and an orbital period,  $P$ , the orbital motion during the planetary deviation causes a shift in the planetary lens position with respect to the source of order

$$\Delta u \approx \Delta t \frac{2\pi}{P} \approx 0.002 - 0.02 , \quad (1.20)$$

assuming a planetary deviation duration of 1–10 days. In order to determine whether eq. 1.20 indicates that the effect of orbital motion is detectable, we need to know what value of  $\Delta u$  is measurable. One thing that limits our resolution in  $\Delta u$  is the finite angular size of the source star. The typical angular size for a bulge main sequence source is  $\theta_* \sim 0.5 \mu\text{as}$  and a typical angular Einstein radius for a bulge event is  $\theta_E \sim 0.5 \text{ mas}$ , so the source radius is typically of order  $\rho = \theta_*/\theta_E \sim 0.001$ . So, if we can detect  $\Delta u$  as small as  $0.1\rho$ , then we could be sensitive to  $\Delta u \sim 10^{-4}$ .

In practice, it can be difficult to do this well in the measurement of orbital effects because changes in other model parameters can often compensate for the change in  $\Delta u$  due to orbital motion. In order to retain a constraint on the orbital motion, it is generally necessary to have a relatively complicated planetary deviation with more than a single caustic crossing or cusp passage that is well sampled by the data. Finally, for events with relatively long planetary signals, the orbital acceleration can be as large as  $\Delta u \approx (\Delta t 2\pi/P)^2 \approx 4 \times 10^{-4}$ . So, with a very well sampled planetary deviation it is also possible to measure the orbital acceleration, as well as the velocity.

## 1.5 Observational Programs

There are a variety of different observing programs that contribute to the detection of planets via gravitational microlensing. The most basic requirement is to be able to identify microlensing events, as was first done by the MACHO Collaboration towards the LMC (Alcock et al., 1993) and OGLE group toward the Galactic bulge (Udalski et al., 1993). Because microlensing observing programs do not yet have the resources to observe  $\gtrsim 10$  square degrees of the Galactic bulge several times per hour, it has been necessary to follow a strategy first suggested by Gould & Loeb (1992). Stellar microlensing events must be identified in progress, and then followed with a global network of telescopes on an  $\sim$ hourly time scale. The MACHO (Alcock et al., 1994, 1996) and OGLE (Udalski et al., 1994) groups developed real-time microlensing detection systems within a year after the first microlensing events were discovered, and this led to the first spectroscopic confirmation of a microlensing event (Benetti et al., 1995). The MOA group began real time detections in 2000 (Bond et al., 2001) and was the first group to employ real time event detection with the more advanced difference imaging photometry method (Bond et al., 2002a).

The first microlensing follow-up projects were the Probing Lensing Anomalies NETwork or PLANET group (Albrow et al., 1998) and the Global Microlensing

Alert Network, or GMAN, (Pratt et al., 1995), which both began taking data in 1995. The PLANET team followed the Gould & Loeb (1992) strategy, but the GMAN group focused more on non-planetary microlensing. A second follow-up group focused on exoplanets, the Microlensing Planet Search (MPS) collaboration began in 1997 (Rhie et al., 1999), but MPS merged with PLANET in 2004. The final microlensing follow-up group is the Microlensing Follow-up Network or MicroFUN (Yoo et al., 2004), which began observations in 2003. MicroFUN does not follow the Gould & Loeb (1992) strategy, but instead focuses on high magnification microlensing events as suggested by Griest & Safizadeh (1998).

### 1.5.1 Early Observational Results

The most definitive of the early planetary microlensing observational results involved limits on the presence of planets based on the lack of detection of planetary signals. The MPS and MOA groups reported the first planetary limits from a high magnification event (Rhie et al., 2000). This, was the first demonstration of sensitivity to Earth-mass planets by any method, except for pulsar timing (Wolszczan & Frail, 1992). The PLANET group followed with limits from a lower magnification event (Albrow et al., 2000b) and then a systematic analysis of five years worth of null detections (Albrow et al., 2001; Gaudi et al., 2002). They found that less than 33% of the lens stars in the inner Galactic disk and bulge have companions of a Jupiter mass or greater between 1.5 and 4 AU. These papers claim that their limits apply to Galactic bulge M-dwarfs, but this summary of the PLANET result neglects an important bias in the events that have been searched for planets. The microlensing teams are more efficient at finding long time scale microlensing events (Alcock et al., 2000a; Sumi et al., 2003; Popowski et al., 2005; Sumi et al., 2006; Hamadache et al., 2006). The long events are also more likely to be discovered prior to peak magnification, so they can be more efficiently searched for planetary signals. As a result, the median time scale of the events search for planets in Gaudi et al. (2002) is  $\langle t_E \rangle = 37$  days, while the actual efficiency corrected median time scale is  $\langle t_E \rangle = 16$  days. This implies that the events that have been searched for planets have more massive lens stars and are more likely to reside in the disk than the typical Galactic bulge microlensing event. Thus, it is probably the case that most of the events searched by Gaudi et al. (2002) have lens stars that are more massive than an M-dwarf, reside in the Galactic disk, or both.

In addition to these upper limits on the planetary frequency, there were also a number of less-than-certain planet detections. Rhie & Bennett (1996) showed that the very first microlensing event discovered showed a light curve feature that could be explained by a planet, but there was a near equal mass binary lens fit that could also explain the data. The MACHO group (Bennett et al., 1997) pointed out that there is a good chance that event MACHO-95-BLG-3 was caused by a free-floating Jupiter-mass planet. The MPS group found that their data for MACHO-97-BLG-41 was best explained by a Jupiter-mass planet orbiting a binary star system (Bennett et al., 1999), but the PLANET data for this event favored an orbiting binary star interpretation (Albrow et al., 2000a). (Some of the MPS data are now known to

be contaminated by moonlight reflecting off the telescope optics.) An analysis by the MOA group (Bond et al., 2002b) showed that the combined MACHO, MOA, MPS, and PLANET data for MACHO-98-BLG-35 was consistent with the low S/N detection of a terrestrial planet. Finally, Jaroszynski & Paczyński (2002) showed that the event OGLE-2002-BLG-55 had a signal consistent with a planet detection, but Gaudi & Han (2004) pointed out that there were other possible explanations.

**Table 1.1.** Exoplanets Discovered by Microlensing

Event Name	Star Mass	Planet Mass	Semi-Major Axis	Lead Group
OGLE-2003-BLG-235Lb/ MOA-2003-BLG-53Lb	$0.63^{+0.07}_{-0.09} M_{\odot}$	$830^{+250}_{-190} M_{\oplus}$	$4.3^{+2.5}_{-0.8} \text{ AU}$	MOA
OGLE-2005-BLG-71Lb	$0.46 \pm 0.04 M_{\odot}$	$1100 \pm 100 M_{\oplus}$	$4.4 \pm 1.8 \text{ AU}$	OGLE
OGLE-2005-BLG-390Lb	$0.22^{+0.21}_{-0.11} M_{\odot}$	$5.5^{+5.5}_{-2.7} M_{\oplus}$	$2.6^{+1.5}_{-0.6} \text{ AU}$	PLANET
OGLE-2005-BLG-169Lb	$0.49^{+0.14}_{-0.18} M_{\odot}$	$13^{+4}_{-5} M_{\oplus}$	$3.2^{+1.5}_{-1.0} \text{ AU}$	MicroFUN
OGLE-2006-BLG-109Lb	$0.50 \pm 0.05 M_{\odot}$	$226 \pm 25 M_{\oplus}$	$2.3 \pm 0.2 \text{ AU}$	MicroFUN
OGLE-2006-BLG-109Lc	$0.50 \pm 0.05 M_{\odot}$	$86 \pm 10 M_{\oplus}$	$4.6 \pm 0.5 \text{ AU}$	MicroFUN

### 1.5.2 Microlensing Planet Detections

Table 1.1 summarizes the properties of the planets discovered by microlensing to date, including four published microlensing exoplanet discoveries (Bond et al., 2004; Udalski et al., 2005; Beaulieu et al., 2006; Gould et al., 2006) plus a 2-planet system that will soon be published (Gaudi et al. 2008, Bennett et al. 2009, in preparation). The microlensing discoveries are compared to other known exoplanets in Fig. 1.9.

The first planet discovered by microlensing is shown in Fig. 1.10. The light curve is plotted in units of the source star flux, which is determined by the best microlensing model to the event, because the star field is too crowded to determine the unmagnified stellar flux directly. This event was first discovered by the OGLE group and announced via their “early warning system” as event OGLE-2003-BLG-235 on 2003 June 22. On 2003 July 21, the alert system of the MOA-I microlensing survey detected this event and reported it as MOA-2003-BLG-53. The MOA detection came later because the MOA-I telescope had only a 0.61 m aperture and has worse seeing conditions than are typical at the 1.3 m OGLE telescope in Chile. However, the MOA telescope had a larger field-of-view (FOV), and this enabled them to image each of their survey fields  $\sim 5$  times per clear night. As a result, MOA was able to detect the second caustic crossing for this event, and arrange for the additional observations that caught the caustic crossing endpoint (thanks to first author, Ian Bond, who was monitoring the photometry in real time).

The naming convention for planets discovered is that the name from the first team to find the microlensing event is used for the event, so in this case OGLE-

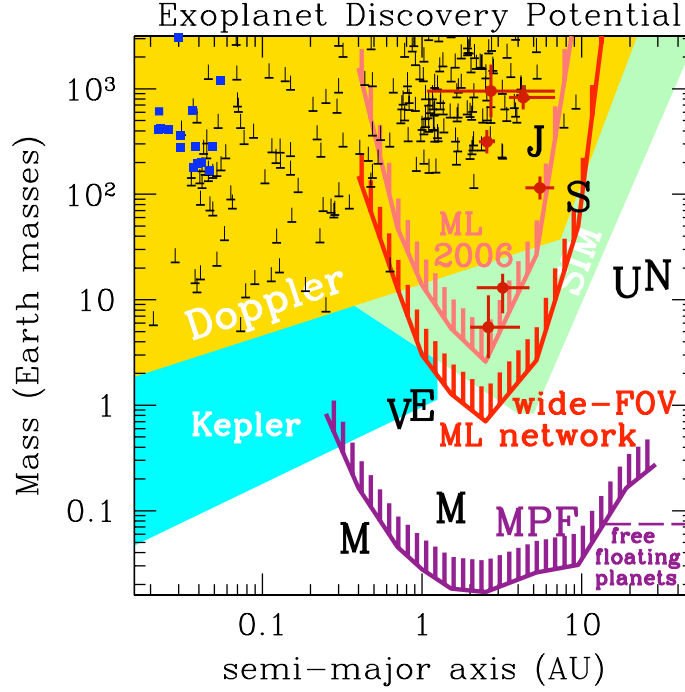


**Fig. 1.9.** The sensitivity of various exoplanet detection methods is plotted in the mass vs. semi-major axis plane. Doppler radial velocity detections are shown in black, with 1-sided error bars for the  $m \sin i$  uncertainty. Planets first detected by transits are shown in blue, and the microlensing planet discoveries are shown in red. The gold, cyan and green shaded regions show the sensitivity of the radial velocity method and NASA’s Kepler and SIM missions, respectively. The light red and red curves show the sensitivity of current and future microlensing planet search programs, and the purple curve gives the sensitivity of the proposed Microlensing Planet Finder (MPF) mission.

2003-BLG-235 takes precedence over MOA-2003-BLG-53. When referring to the lens system, we add a suffix “L”, and when referring to the source, we add an “S”. For a lens or source system that is multiple, we add an additional capital letter suffix for a stellar mass object or a lower case letter for a planetary mass companion. So, OGLE-2006-BLG-109LA, OGLE-2006-BLG-109Lb, and OGLE-2006-BLG-109Lc, refer to the star and two known planets of the OGLE-2006-BLG-109 lens system. This convention provides names for multiple components of the source star system. For example, OGLE-2022-BLG-876Sb would refer to a planetary companion to the source star (which would be difficult, but not impossible (Graff & Gaudi, 2000; Lewis, 2001) to detect).

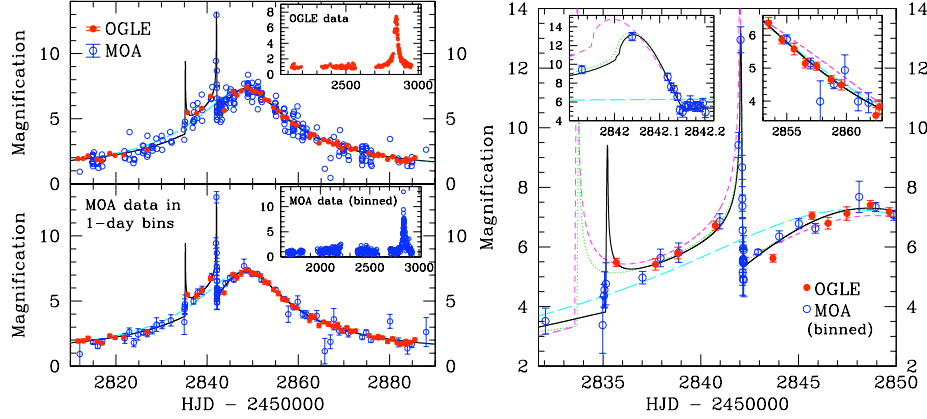


**Fig. 1.10.** The OGLE-2003-BLG-235/MOA-2003-BLG-53 light curve with OGLE data in red and MOA data in blue. The top-left panel presents the complete data set during 2003 (main panel) and the 20012003 OGLE data (inset). The median errors in the OGLE and MOA points are indicated in the legend. The bottom panel is the same as the top panel, but with the MOA data grouped in 1 day bins, except for the caustic crossing nights, and with the inset showing MOA photometry during 20002003. The binary- and single-lens fits are indicated by the solid black and cyan dashed curves, respectively. The right panel shows the light curve and models during caustic traverse. These models are the single-lens case (*cyan, long-dashed curve*), the best binary lens with  $q \gtrsim 0.03$  (*magenta, short-dashed line*), the planetary lens with caustic entry before day 2835 (*green, dotted line*), and the best overall fit with  $q = 0.0039$  (*black, solid line*). The insets show the second caustic crossing and a region of the declining part of the light curve where the best-fit nonplanetary binary-lens model fails to fit the data. MOA data on days other than the caustic entry and exit (days  $2835 \pm 0.5$  and  $2842 \pm 0.5$ ) are placed in 1 day bins.

It is interesting to note that this event was discovered by a procedure that differs from both the alert-plus-followup strategy suggested by Gould & Loeb (1992) and the high magnification strategy suggested by Griest & Safizadeh (1998). Instead, the planetary deviation was detected in the observations of one of the survey teams, and identified in time to obtain additional data to confirm the planetary nature of the light curve deviation. We will return to this strategy later in the discussion of future microlensing projects given in § 1.6.

Another notable feature of this event is that the lens star has been identified in HST images (Bennett et al., 2006). As indicated in Fig. 1.7, there is an extra source of light superimposed at the location of the source star. This is very likely to be the lens star, and if so, the HST photometry implies that a fraction,  $f_{\text{lens}} = 0.18 \pm 0.05$ , of the total source plus lens flux comes from the lens. During the microlensing event, the lens and source were separated by  $< 0.1$  mas, but by the time of the HST images,  $\Delta t = 1.78$  years after peak magnification, the lens-source separation should have grown to  $\Delta t \mu_{\text{rel}} = 5.9 \pm 0.7$  mas. ( $\mu_{\text{rel}} = 3.3 \pm 0.4$  mas/yr was determined

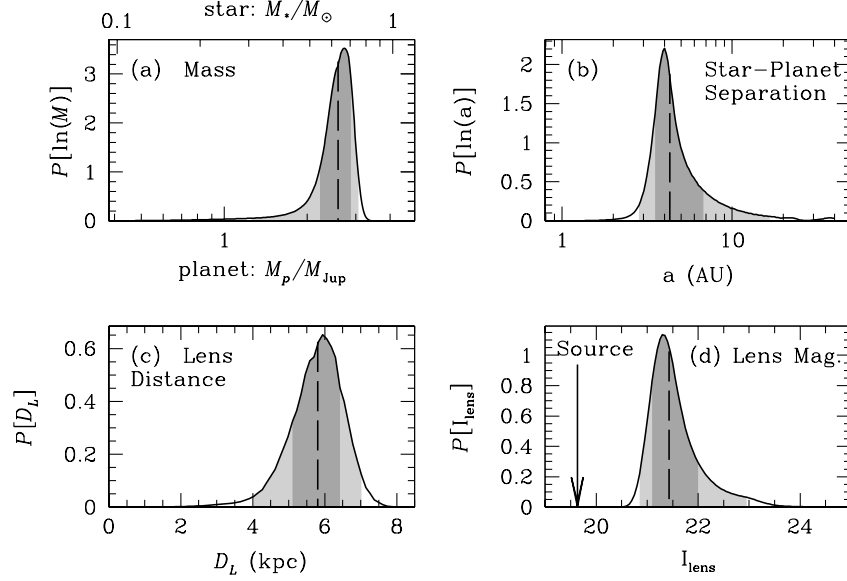


**Fig. 1.11.** Bayesian probability densities for the properties of the planet, OGLE-2003-BLG-235Lb, and its host star if it is a main sequence star. (a) The masses of the lens star and its planet ( $M_*$  and  $M_p$  respectively). (b) the separation, (c) their distance from the observer ( $D_L$ ); and (d) the I-band brightness of the host star. The dashed vertical lines indicate the medians, and the shading indicates the central 68.3% and 95.4% confidence intervals. All estimates follow from a Bayesian analysis assuming a standard model for the disk and bulge population of the Milky Way, the stellar mass function of Bennett & Rhie (2002).

from eq. 1.16 with input parameters from the light curve model.) This separation, plus the mass-distance relation, eq. 1.17, enable to derivation of the curves shown in the bottom left panel of Fig. 1.7. These show the amplitude for the offset of the centroids of the blended lens plus source images in different color bands. The HST data indicate a marginal detection of this color-dependent centroid shift at a level consistent with the assumption that the excess flux is due to the lens.

With this marginal detection of the color-dependent centroid shift, we can't be absolutely sure that the lens star has been detected because it is possible that the excess flux could be due to a companion to the source star. It is straight forward to deal with this uncertainty with a Bayesian analysis (Bennett et al., 2006), and the results of such an analysis are shown in Fig. 1.11. The resulting most likely parameter values for the event parameters are a host star mass of  $M_* = 0.63^{+0.07}_{-0.09} M_\odot$ , a planet mass of  $M_p = 2.6^{+0.8}_{-0.6} M_{\text{Jup}}$ , and an orbital semi-major axis of  $a = 4.3^{+2.5}_{-0.8}$  AU. The distance to the lens system is  $D_L = 5.8^{+0.6}_{-0.7}$  kpc, and the lens star magnitude is  $I_L = 21.4^{+0.6}_{-0.3}$ .



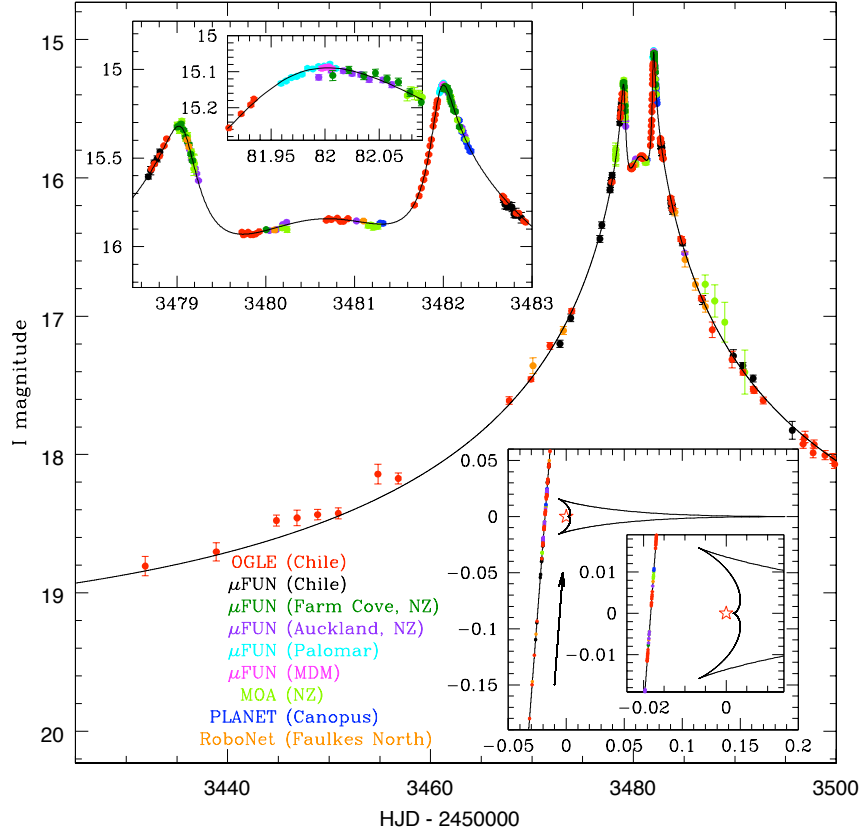


**Fig. 1.12.** The OGLE-2005-BLG-71 light curve showing the planetary anomaly near the peak. The triple peak (two large symmetric peaks surrounding a small peak) indicates that the source passed three cusps of a caustic, the middle one being weak (*insets*). The interval between peaks (and so cusps) is  $\Delta t = 3$  days, implying that the companion mass must be small.

The light curve of the second planet discovered by microlensing, OGLE-2005-BLG-71Lb, is shown in Fig. 1.12 (Udalski et al., 2005). This was a moderately high magnification event that would have reached a maximum magnification of  $A_{\max} \approx 42$  if the lens star had no planets. Because of the  $d \leftrightarrow 1/d$  ambiguity discussed in § 1.4, this event has two models that explain the major features of the light curve quite well. Fig. 1.3 shows the magnification patterns for these models, and for the trajectory of the lens, which is nearly perpendicular to the lens axis, the light curves for these different models are quite similar. From Udalski et al. (2005) the physically interesting parameters of the best fit models are  $t_E = 70.9 \pm 3.3$ ,  $q = 7.1 \pm 0.3 \times 10^{-3}$ , and  $d = 1.294 \pm 0.002$  for the “wide” model and  $t_E = 73.9 \pm 3.5$ ,

$q = 6.7 \pm 0.3 \times 10^{-3}$ , and  $d = 0.758 \pm 0.002$  for the “close” model. However, the  $\chi^2$  difference between these two models is  $\Delta\chi^2 = \chi^2_{\text{close}} - \chi^2_{\text{wide}} = 22.0$ , so the “wide” model is strongly preferred.

OGLE-2005-BLG-71Lb was the first planet discovery with significant contributions from amateur astronomers, with critical observations near the two strong cusp approach peaks by Grant Christie of the Auckland Observatory and Jennie McCormick of the Farm Cove Observatory.

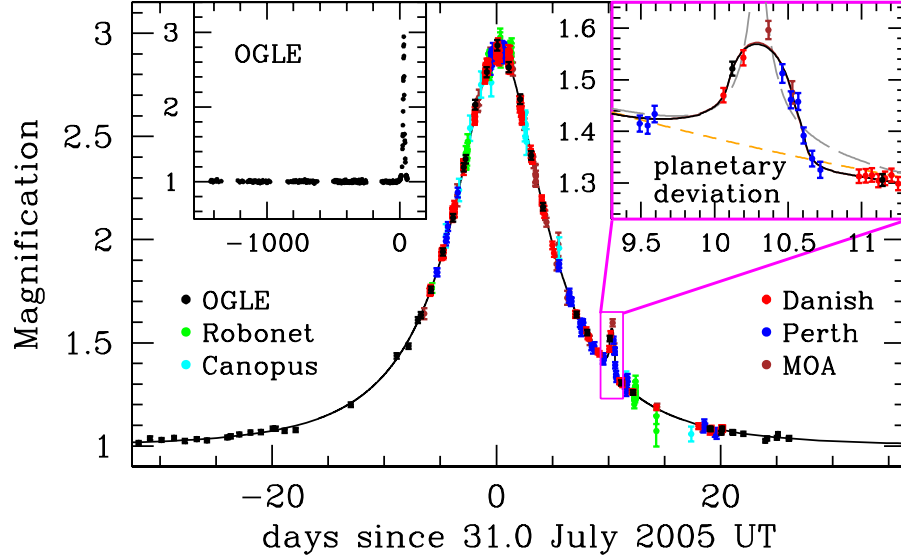


**Fig. 1.13.** The observed light curve of the OGLE-2005-BLG-390 microlensing event and best-fit model plotted as a function of time. The data set consists of 650 data points from PLANET Danish (*red points*), PLANET Perth (*blue*), PLANET Canopus (Hobart, *cyan*), RoboNet Faulkes North (*green*), OGLE (*black*), and MOA (*brown*). The top left inset shows the OGLE light curve extending over the previous 4 years, whereas the top right one shows a zoom of the planetary deviation, covering a time interval of 1.5 days. The solid curve is the best binary lens model described in the text with  $q = 7.6 \pm 0.7 \times 10^{-5}$ , and a projected separation of  $d = 1.610 \pm 0.008 R_E$ . The dashed grey curve is the best binary source model that is rejected by the data, and the dashed orange line is the best single lens model.

With a mass ratio of  $q = 7.1 \pm 0.3 \times 10^{-3}$ , OGLE-2005-BLG-71Lb must certainly be a gas giant planet, but without further information such as measurement of finite source effects, the detection of the lens star or a measurement of the microlensing parallax effect, we cannot determine the properties of the host star or the planetary mass with much precision. Fortunately, we are able to detect lens star in a set of HST images, and the light curve yields weak detections of both a finite source size

and the microlensing parallax effect. So, we expect to determine the host star and planet masses and to convert their separation into physical units, but this analysis is not yet complete (Dong et al 2007, in preparation).

The first low-mass planet discovered by microlensing was OGLE-2005-BLG-390Lb (Beaulieu et al., 2006), led by the PLANET Collaboration. This planet is currently tied with Gl 581c (Udry et al., 2007) as the lowest mass exoplanet orbiting a normal star yet to be discovered<sup>1</sup>. This event was detected through a planetary caustic deviation, and the amplitude of the deviation was significantly reduced by the finite angular size of the clump giant source star. If the planet were smaller by a factor of  $\sim 2$ , it would not have been detected in this event. As originally pointed out in Bennett & Rhie (1996) and discussed in § 1.3.3, a microlensing search for Earth-mass planets should focus on events with main sequence source stars.

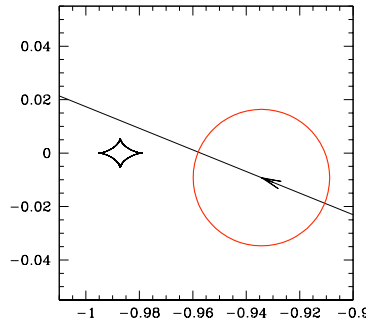


**Fig. 1.14.** Comparison of the OGLE-2005-BLG-390Lb planetary caustic (*the black diamond shaped curve*) with the source star size (*red circle*). The black line with the arrow show the motion of the source star.

The OGLE-2005-BLG-390Lb light curve deviation does not show the characteristic features of a fold caustic crossing, like OGLE-2003-BLG-235, or of a cusp approach, like OGLE-2005-BLG-71. This is because the planetary caustic is smaller than the source star's angular radius of  $\theta_* = 5.3 \pm 0.7 \mu\text{as}$  is larger than the planetary caustic, as shown in Fig. 1.14. Because the light curve does not show these characteristic binary-microlensing features, we must consider a non-planetary explanation for the light curve involving the lensing of a binary source star by a single star lens. Gaudi (1998). However, as the Fig. 1.13 shows, a binary source model is a poor fit to the data, as it fails to account for the Perth and Danish data near the end of the perturbation. Formally, the binary source model increases the fit  $\chi^2$  by  $\Delta\chi^2 = 46.25$  with one fewer degree of freedom. These data are also sufficient to

<sup>1</sup> The minimum mass of  $M_p \geq 5.03M_\oplus$  is often quoted for Gl 581c, but the  $M_p \sin i$  ambiguity of the radial velocity method implies that the median predicted mass is  $M_p = 5.5M_\oplus$ . This is the appropriate number to compare to other detection methods.

avoid a possible degeneracy in the planetary parameters for such events that occurs when the wings of the deviation are poorly sampled (Gaudi & Gould, 1997).

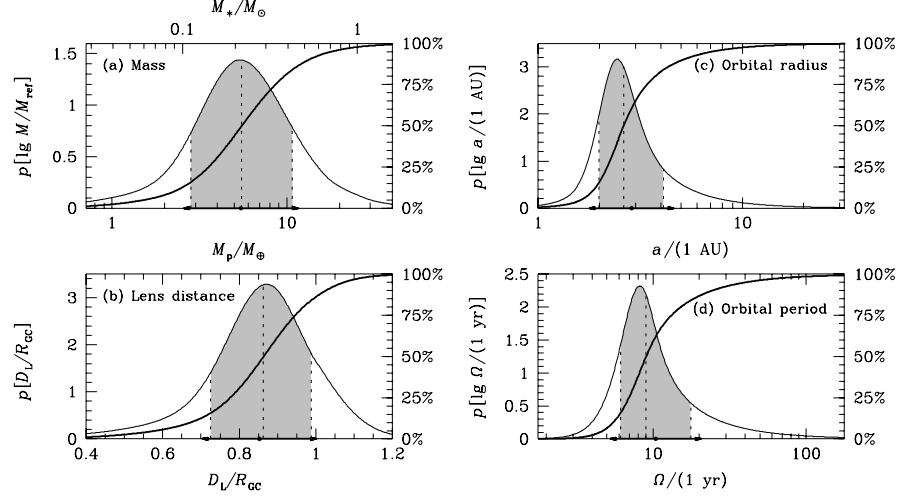


**Fig. 1.15.** Bayesian probability densities for the properties of the planet and its host star: (a), the masses of the lens star and its planet ( $M_*$  and  $M_p$  respectively), (b), their distance from the observer  $D_L$ , (c), the three dimensional separation or semi-major axis  $a$  of an assumed circular planetary orbit; and (d), the orbital period  $\Omega$  of the planet. The bold, curved line in each panel is the cumulative distribution, with the percentiles listed on the right. The dashed vertical lines indicate the medians, and the shading indicates the central 68.3% confidence intervals, while dots and arrows on the abscissa mark the expectation value and standard deviation. The medians of these distributions yield a  $M_p = 5.5^{+5.5}_{-2.7} M_\oplus$  planetary companion at a separation of  $d = 2.6^{+1.5}_{-0.6}$  AU from a  $M_* = 0.22^{+0.21}_{-0.11} M_\odot$  Galactic Bulge M-dwarf at a distance of  $D_L = 6.6 \pm 1.0$  kpc from the Sun. The median planetary period is  $\Omega = 9^{+9}_{-3}$  years.

The microlensing model for this event directly determines the planetstar mass ratio,  $q = 7.6 \pm 0.7 \times 10^{-5}$ , the projected planetstar separation,  $d = 1.610 \pm 0.008$ , the Einstein radius crossing time,  $t_E = 11.03 \pm 0.11$  days, and the source radius crossing time,  $t_* = 0.282 \pm 0.010$  days. With the value for  $\theta_*$  mentioned above, this yields the angular Einstein radius,  $\theta_E = 0.21 \pm 0.03$  mas, from eq. 1.16 and the mass-distance relation from eq. 1.17. This mass-distance relation can be combined with a standard Galactic model in a Bayesian analysis to estimate the probability distribution of the lens system parameters (Alcock et al., 1995, 1996; Poindexter et al., 2005; Dominik, 2006). The results of such an analysis are shown in Fig. 1.15 following the method of Dominik (2006), and nearly identical results are obtained using the Galactic model and mass function parameters of Bennett & Rhie (2002). This analysis gives a 95% probability that the planetary host star is a main-sequence star, a 4% probability that it is a white dwarf, and a probability of 1% that it is a

neutron star or black hole. The median parameters shown in Fig. 1.15 imply that the planet receives radiation from its host star that is only 0.1% of the radiation that the Earth receives from the Sun, so the probable surface temperature of the planet is 50 K, similar to the temperature of Neptune.

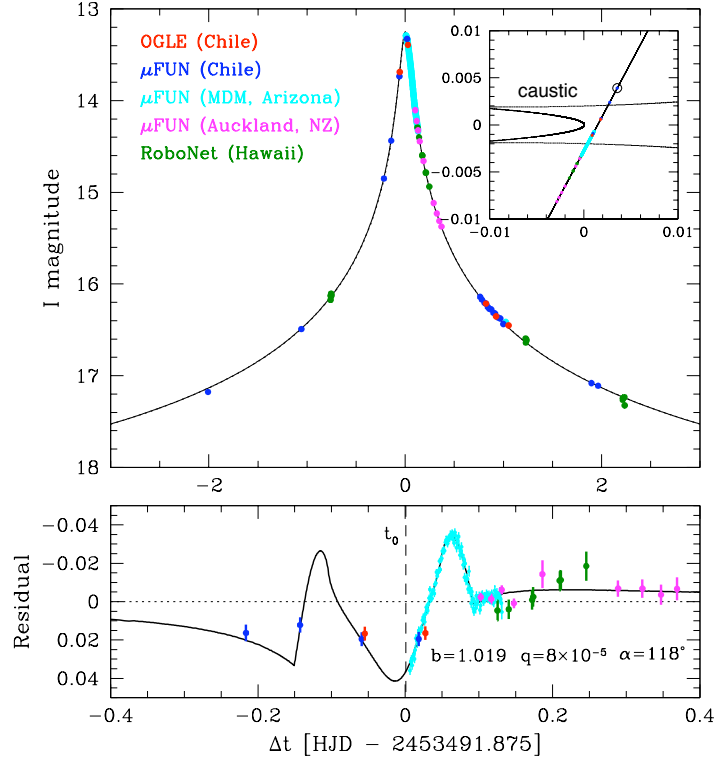


**Fig. 1.16.** *Top:* Data and best-fit model for OGLE-2005-BLG-169. *Bottom:* Difference between this model and a single-lens model with the same single lens parameters ( $t_0$ ,  $u_0$ ,  $t_E$ , and  $\rho$ ). It displays the classical form of a caustic entrance/exit that is often seen in binary microlensing events, where the amplitudes and timescales are several orders of magnitude larger than seen here. MDM data trace the characteristic slope change at the caustic exit ( $\Delta t = 0.092$ ) very well, while the entrance is tracked by a single point at  $\Delta t = -0.1427$ . The dashed line indicates the time  $t_0$ . *Inset:* Source path through the caustic geometry. The source size,  $\rho$ , is indicated.

As discussed in § 1.4.1, the lens star mass can be determined directly if the lens star is detected. However, this will be quite difficult for OGLE-2005-BLG-390L, because the source is a giant star. For the median mass and distance to the lens system, the lens star would be fainter than the source by a factor of 2000 in the

$K$ -band. So, the detection of the lens star may require many years for the relative proper motion of  $\mu_{\text{rel}} = 6.8 \text{ mas/yr}$  and the development of new instruments for large ground-based or space telescope.

OGLE-2005-BLG-169 was the third published event from the 2005 season and the second low-mass planet found by microlensing (Gould et al., 2006). This was a very high magnification event, with a peak magnification of  $A_{\text{max}} \simeq 800$ , and its light curve is shown in Fig. 1.16. The bottom panel of Fig. 1.16 indicates that the planetary deviation has a maximum amplitude of about 4% compared to the light curve of the same event without a planet. Such low amplitude deviations characteristic of the very weak caustics due to low-mass planets near the Einstein ring. However, it is only part of the caustic curve that is so weak. If the source would have passed on the other side of the host star and crossed the backwards “C” shaped part of the caustic in the inset of Fig. 1.16, the planetary signal would have been very much stronger. But, in order to detect the low amplitude signal due to the caustics actually crossed by the source star, it was quite helpful to have continuous observations over the course of three hours from the 2.4 m MDM telescope.

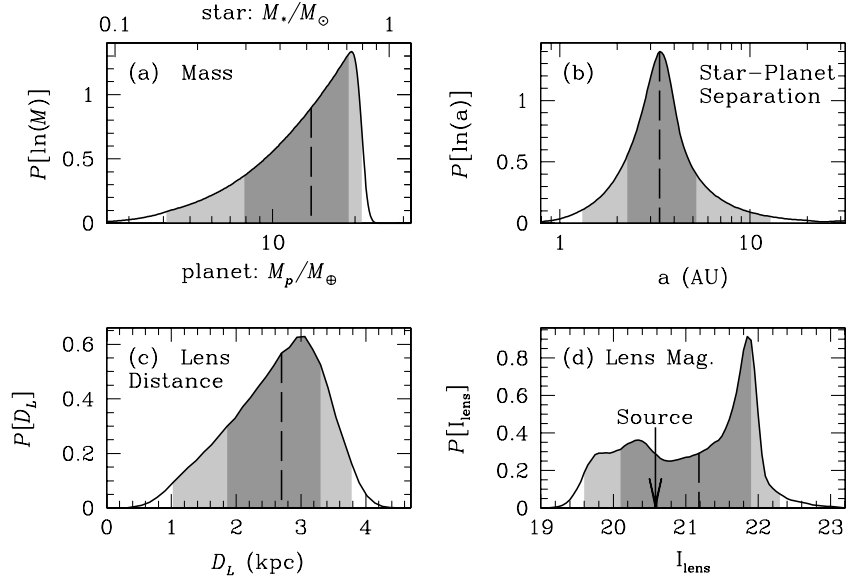


**Fig. 1.17.** OGLE-2005-BLG-169 lens property figure. Bayesian probability densities for the properties of the planet and its host star if it is a main sequence star. (a) The masses of the lens star and its planet ( $M_*$  and  $M_p$  respectively). (b) the separation, (c) their distance from the observer ( $D_L$ ); and (d) the I-band brightness of the host star. The dashed vertical lines indicate the medians, and the shading indicates the central 68.3% and 95.4% confidence intervals. All estimates follow from a Bayesian analysis assuming a standard model for the disk and bulge population of the Milky Way, the stellar mass function of Bennett & Rhie (2002).

The analysis of Gould et al. (2006) indicated a super-Earth mass planet with  $M_p = 13^{+6}_{-8} M_\oplus$  orbiting a star of  $M_* \simeq 0.49 M_\odot$ . Such a planet, like OGLE-2005-BLG-390Lb, would be invisible to other planet detection methods. High magnification events also place tight constraints on the presence of additional planets, and in the case of OGLE-2005-BLG-169, Jupiter-mass planets can be excluded from the separation range 0.6-18 AU and Saturn-mass planets can be excluded from the range 1-11 AU.

The precise masses of the host star and planet have not yet been determined because the host star has not been detected. Thus, the lens system properties can only be determined by a Bayesian analysis, as was done for OGLE-2005-BLG-390Lb in Fig. 1.15. This analysis uses the parameters from the microlensing light curve, including the Einstein radius crossing time of  $t_E = 43 \pm 1.3$  days, the source radius crossing time of  $t_* = 0.019 \pm 0.01$  days, and the lens-source relative proper motion of  $\mu_{\text{rel}} = 8.4 \pm 0.6$  mas/yr. The results of this analysis are presented in Figure 1.17. These have assumed a Han-Gould model for the Galactic bar (Han & Gould, 1995), a double-exponential disk with a scale height of 325 pc, and a scale length of 3.5 kpc, as well as other Galactic model parameters as described in Bennett & Rhie (2002). Because this model is different from the Galactic model used by Gould et al. (2006), the resulting parameters differ slightly from their results. We find a lens system distance of  $D_L = 2.7^{+0.6}_{-0.9}$  kpc, a three dimensional star-planet separation of  $a = 3.3^{+1.9}_{-0.9}$  AU and main sequence stellar and planetary masses of  $M_* = 0.52^{+0.19}_{-0.22} M_\odot$  and  $M_p = 14^{+5}_{-6} M_\oplus$ . If we assume that white dwarfs have an *a priori* probability to host planets that is equal to that of main sequence stars (at the separations probed by microlensing), then there is a 35% probability that the host star is a white dwarf. The possibility of a brown dwarf host star is excluded by the light curve limits on the microlensing parallax effect (Gould et al., 2006).

Fig. 1.17(d) shows the probability distribution of the *I*-band magnitude of the planetary host star compared to the source star at  $I = 20.58 \pm 0.10$ . The implied planetary host star brightness distribution has a median and 1- $\sigma$  range of  $I_{\text{lens}} = 21.9^{+0.7}_{-1.1}$ , but the most interesting feature of this figure is that the probability of a main sequence lens fainter than  $I = 23$  vanishes. This is because the mass-distance relation, eq. 1.17 ensures that the lens star will be nearby and at least as bright as  $I = 23$ , even if it is at the bottom of the main sequence at  $M_* = 0.08 M_\odot$ . In fact, the microlensing parallax constraint from the light curve yields a lower limit for the lens star mass of  $M_* \gtrsim 0.14 M_\odot$ . Thus, the planetary host star must be at least 16% of the brightness of the combined lens plus source star blended image, and this implies that it will be detectable if it is not a stellar remnant. Plus, the relatively rapid relative proper motion,  $\mu_{\text{rel}} = 8.4 \pm 0.6$  mas/yr, of OGLE-2005-BLG-169L, implies that the lens-source separation is already detectable with HST (Bennett et al., 2007a), as discussed in § 1.4.1.

One of the most interesting consequences of the discoveries of OGLE-2005-BLG-390Lb and 169Lb is that super-earth planets of  $\sim 5\text{-}15 M_\oplus$  are likely to be quite common. Gould et al. (2006) combined these detections with null results from very high magnification events (Abe et al., 2004; Dong et al., 2006) plus samples of

lower magnification events (Albrow et al., 2001; Gaudi et al., 2002) to solve for the fraction,  $f_{\text{se}}$ , of stars with planets of mass ratio  $\sim 8 \times 10^{-5}$  at the separations of 1.5-4 AU, where microlensing is most sensitive. They found that the median and 90% confidence level upper and lower limits are  $f_{\text{se}} = 0.38^{+0.31}_{-0.22}$ , based on the two planets discovered and the accumulated null results. The 90% c.l. lower limit is  $f_{\text{se}} \geq 16\%$ . This is significantly higher than the fraction of F, G, and K stars with Jupiter-mass planets in this 1.5-4 AU separation range. This fraction of stars with Jupiters at this separation can be estimated from Butler et al. (2006) to be  $f_{\text{J}} \simeq 3\%$ . Thus, these cool, super-earth planets appear to represent the most common type of exoplanet yet discovered. This would seem to confirm the prediction of the core-accretion theory that  $\sim 10M_{\oplus}$  planets form much more frequently than gas giants, like Jupiter (Ida & Lin, 2004; Laughlin, Bodenheimer & Adams, 2004), although this may not be incompatible with the disk instability theory (Boss, 2006).

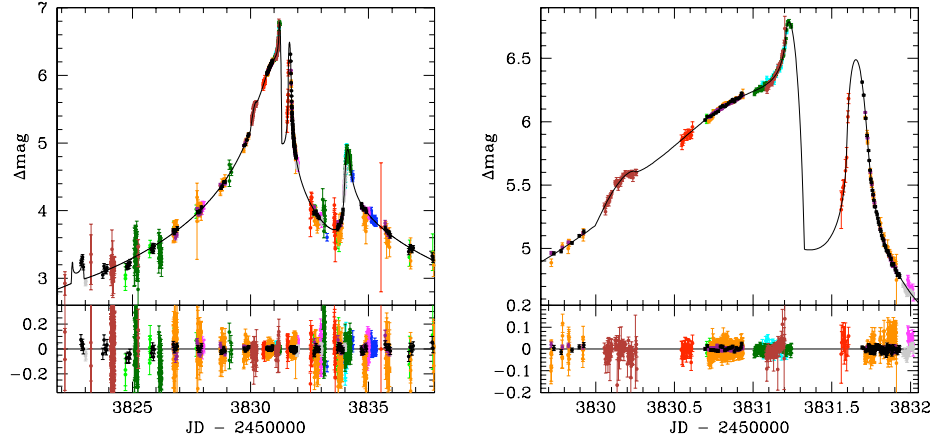


**Fig. 1.18.** Two views of the OGLE-2006-BLG-109 light curve, which is the first multi-planet microlensing event with a planet of slightly less than a Jupiter mass ( $q = 1.35 \times 10^{-3}$  at  $\sim 2.7$  AU and a planet of slightly more than a Saturn mass ( $q = 4.9 \times 10^{-4}$ ) at  $\sim 5.4$  AU. The signal is dominated by the Saturn-mass planet because it is close to the Einstein ring at  $d = 1.4$ , and there are two pairs of caustic crossing features (at  $t = 3822.5$ ,  $3822.9$  and  $t = 3830.2$ ,  $3831.2$ ) and a cusp approach (at  $t = 3834.1$ ) due to the Saturn-mass planet. The Jupiter-mass planet is further from the Einstein ring at  $d = 0.63$ , so its signal is limited to the highest magnification part of the light curve and is responsible for the cusp approach feature at  $t = 3831.65$ . Both planetary orbital motion and microlensing parallax must be included to obtain an acceptable model for this event.

The final event that we will present is OGLE-2006-BLG-109, which is much more complicated than the other events (Gaudi et al. 2007; Bennett et al. 2007, both in preparation). The light curve for this event is shown in Fig. 1.18, while the central caustic configuration is shown in Fig. 1.19. This is the first microlensing event with



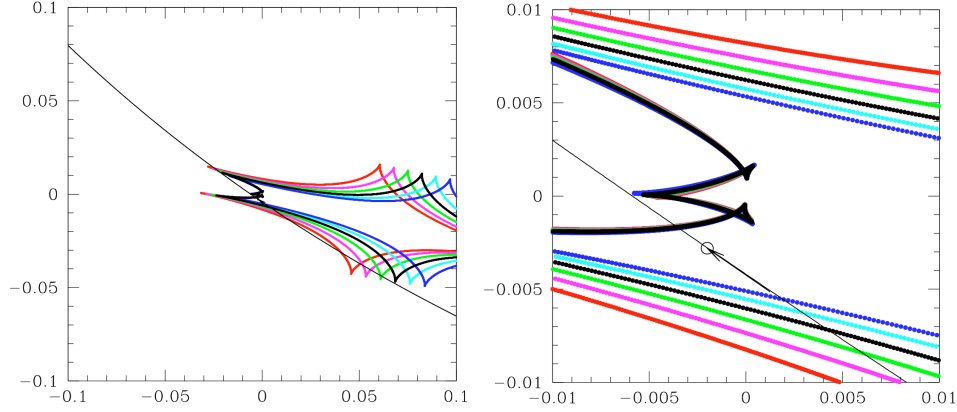


**Fig. 1.19.** The central caustic OGLE-2006-BLG-109 configuration for is shown at 3-day intervals from  $t = 3820$  (shortly before the first caustic crossing) through  $t = 3835$  (a day after the final cusp approach). The time-order of the different color caustic curves is *red, magenta, green, black, cyan, blue*. The grey curve is the source trajectory, which is curved due to the microlensing parallax effect (*i.e.* the orbital motion of the Earth) and the small circle that the source trajectory in the left, close-up panel shows the source star radius.

two detected planets, and it also shows clear signals of planetary orbital motion and microlensing parallax. These effects are detectable because the Saturn-mass planet has a projected separation that is close to the Einstein ring, which causes its caustic to become quite extended. Its effects are visible for 11 days.

Another notable feature of OGLE-2006-BLG-109 is that the lens is  $> 5$  times brighter than the source. It is detectable (although not completely resolved) in the best seeing ( $0.7''$ ) OGLE images and is clearly visible in  $K$  and  $H$ -band adaptive optics images from the Keck telescope. As a result, there are two methods to determine the lens star mass: the combination of the  $\theta_E$  determination from the finite source effects and the microlensing parallax effect yields the lens mass via eq. 1.19, while the lens star detection give the lens mass with the help of mass-luminosity relations, as discussed in § 1.4.1. However, one complication is that there is some degeneracy in the effects of microlensing parallax and the planetary orbital motion on the microlensing light curve. On the other hand, the planetary orbital motion parameters yield information about the orbits that haven't been detected before in a microlensing event. So, this event will yield much more information about the OGLE-2006-BLG-109L planetary system than was anticipated for any planetary microlensing event.

## 1.6 Future Programs

Our experience with the existing microlensing planet search programs provides indications of how the sensitivity of future microlensing surveys can be improved. At

present, the OGLE and MOA groups are each able to independently discover more than 500 microlensing events per year. There is a great overlap between the discoveries of these two groups, but the total number of events discovered every year is probably about 700. This is at least an order of magnitude larger than the global follow-up groups can hope to follow. The follow-up groups optimize their observations by focusing on high magnification events. However, many of the shorter time scale high magnification events are not recognized as such in time, and so a large fraction of the high magnification events are not searched for planets.

The solution to this problem is to observe many microlensing events in each image with a global network of very wide FOV telescopes that can observe 10 square degrees or more of the Galactic bulge at 15-20 intervals. The new 1.8m MOA-II telescope (Hearnshaw et al., 2005) with a 2.2 square degree FOV CCD camera (Yanagisawa et al., 2000) that began operation in 2006 is the first telescope that meets this requirement, and the OGLE group plans to upgrade to a 1.4 square degree OGLE-4 camera in time for the 2009 Galactic bulge observing season. With MOA-II in New Zealand, and OGLE-IV in Chile, all that is needed is a very wide-FOV microlensing survey telescope in Southern Africa. A number of groups are pursuing funding for such a telescope.

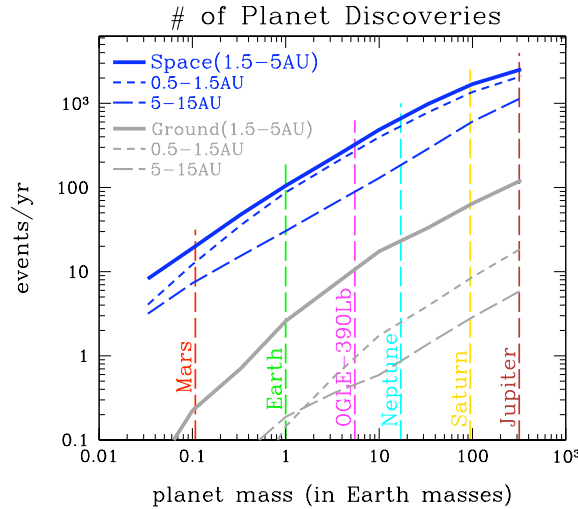


**Fig. 1.20.** The number of planet detections expected per year as a function of planet mass is shown for proposed future space and ground-based microlensing surveys under the assumption of one planet per star in the indicated separation ranges. The space-based survey has its most significant advantage over the ground-based survey at separations smaller (0.5-1.5 AU) and larger (5-15 AU) than the Einstein radius, because a space-based survey is able to resolve bulge main sequence stars and detect moderate amplitude planetary signals when the magnification due to the stellar lens is small.

Simulations of such a system have been performed by Bennett (2004) and Gaudi (2007, private communication), and estimates of the sensitivity of the global network consisting of MOA-II, OGLE-IV and an OGLE-IV-like system in South Africa are presented in Fig. 1.9 and Fig. 1.20. The improvement in sensitivity with such a network in the mass vs. semi-major axis plane is shown in Fig. 1.9 with the light and dark red curves showing the sensitivity of the current surveys and the future very wide-FOV network, respectively. This network will extend the sensitivity of the microlensing method down to an Earth mass at planet-star separations close to the Einstein ring radius ( $\sim 2\text{--}3\text{ AU}$ ).

The separation range where ground-based microlensing is most sensitive, 1-5 AU corresponds to the vicinity of the so-called “snow-line,” which is the region of the proto-planetary disk where it is cold enough for water-ice to condense. The density of solids in the proto-planetary increases by a factor of  $\sim 4$  across the “snow-line,” and as a result, the core accretion theory predicts that this is where the most massive planets will form (Ida & Lin, 2004; Laughlin, Bodenheimer & Adams, 2004; Kennedy et al., 2006). According to this theory, giant planets form just outside the “snow line” where they can accrete  $\sim 10M_{\oplus}$  of rock and ice to form a core that grows into a gas giant like Jupiter or Saturn via the run-away accretion of Hydrogen and Helium onto this core. However, this theory also predicts that the Hydrogen and Helium gas can easily be removed from the proto-planetary disk during the millions of years that it takes to build the rock-ice core of a gas-giant. Thus, if the core accretion theory is correct, rock-ice planets of  $\sim 10M_{\oplus}$  that failed to grow into gas giants should be quite common, although it is possible to form such planets in the competing gravitational instability theory (Boss, 2006).

The number of planetary microlensing event detections expected per year is shown in Fig. 1.20 assuming an average of one such planet per star, with conservative assumptions regarding photometric precision. The assumption of an average of one such planet per star is certainly too optimistic for Jupiter mass planets (Gaudi et al., 2002; Butler et al., 2006), but it is closer to reality for super-earths, like OGLE-2005-BLG-390Lb and OGLE-2005-BLG-169Lb (Beaulieu et al., 2006; Gould et al., 2006). It could very well be accurate for Earth-mass planets where the weaker two-body gravitational interactions allow two planets to orbit in the separation range corresponding to the bins in Fig. 1.20. (Our own solar system is an example of this.)

Another future development that is already funded is a global network of robotic telescopes dedicated to monitoring transient events like planetary microlensing events, known as the Las Cumbres Global Telescope Network (Brown et al., 2007). Ideally, this network would routinely observe high magnification microlensing events and planetary deviations discovered in progress with an very high cadence, such as that provided by the MDM telescope for OGLE-2005-BLG-169 (see Fig. 1.16. This would enable the very wide-FOV survey telescopes to maintain their normal sampling strategy so that other planetary microlensing events would not be missed. This might add to the planet detection efficiency substantially, but such a system is more difficult to model.

### 1.6.1 The Ultimate Exoplanet Census: Space-Based Microlensing

The ultimate census for virtually all types of exoplanets would be a space-based microlensing survey (Bennett & Rhie, 2002; Bennett et al., 2007b). Such a survey could provide a statistical census of exoplanets with masses  $\geq 0.1M_{\oplus}$  and orbital separations ranging from 0.5 AU to  $\infty$ . This includes analogs to all the Solar Systems planets except for Mercury, as well as most types of planets predicted by planet formation theories. This survey would determine the frequency of planets around all types of stars except those with short lifetimes. Close-in planets with separations  $< 0.5$  AU are invisible to a space-based microlensing survey, but these can be found by Kepler (Basri et al., 2005). Other methods, including ground-based microlensing, cannot approach the comprehensive statistics on the mass and semi-major axis distribution of extrasolar planets that a space-based microlensing survey will provide. Detailed simulations of a space-based microlensing survey (Bennett & Rhie, 2002) have been used to determine the sensitivity of such a mission, and Figs. 1.9 and 1.20 show the sensitivity of the proposed Microlensing Planet Finder (MPF) mission (Bennett et al., 2004). These figures also show that the sensitivity of a ground-based microlensing survey to terrestrial planets is limited to the vicinity of the Einstein radius at 2-3 AU. This is because ground-based survey generally requires moderately high magnification  $A \gtrsim 10$  in order to resolve the source star well enough to get the moderately precise photometry that is needed to detect planets with the microlensing method. A space-based microlensing survey would generally resolve the source stars, so planets further from the Einstein radius can be detected via their light curve perturbations at relatively low magnification from the lensing effect of the planetary host star.

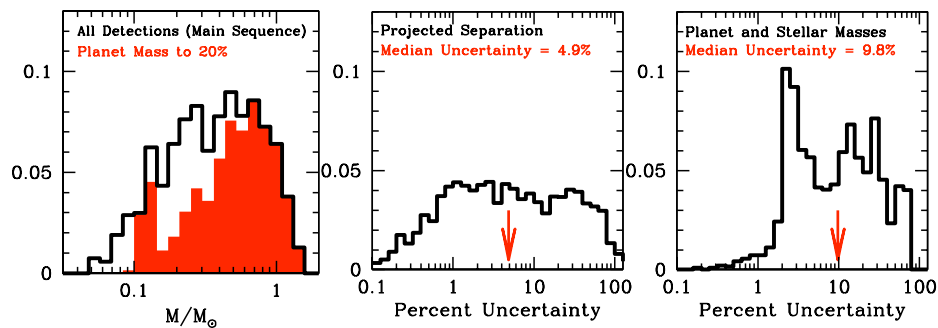


**Fig. 1.21.** (a) The simulated distribution of stellar masses for stars with detected terrestrial planets. The red histogram indicates the subset of this distribution for which the masses can be determined to better than 20%. (b) The distribution of uncertainties in the projected star-planet separation. (c) The distribution of uncertainties in the star and planet masses. Note that it is the two-dimensional projected separation that is presented here, and we have not included the uncertainty in the separation along the line-of-sight as was done in Figure 1.17.

A space-based microlensing survey is also able to detect most of the planetary host stars for most planetary microlensing events. Using the methods described in § 1.4.1 and in more detail in Bennett et al. (2007a), this allows the determination of the star and planet masses and separation in physical units. This can be accomplished with HST observations for a small number of planetary microlensing events (Bennett et al. 2006), but only a space-based survey can do this for hundreds or thousands of planetary microlensing events that future surveys would expect to discover. Fig. 1.17 shows the distribution of planetary host star masses and the predicted uncertainties in the masses and separation of the planets and their host stars (Bennett et al., 2007a) from simulations of the MPF mission. The host stars with masses determined to better than 20% are indicated by the red histogram in Fig. 1.17(a), and these are primarily the host stars that can be detected in MPF images. Ground-based microlensing surveys also suffer significant losses in data coverage and quality due to poor weather and seeing. As a result, a significant fraction of the planetary deviations seen in a ground-based microlensing survey will have poorly constrained planet parameters due to poor light curve coverage (Peale, 2003). (These poorly characterized detections are not included in Fig. 1.20, however.)

Proposed improvements to ground-based microlensing surveys can detect Earth-mass planets in the vicinity of the “snow-line,” which is critical for the understanding of planet formation theories (Gould et al., 2007). But such a survey would have its sensitivity to Earth-like planets limited to a narrow range of semi-major axes, so it would not provide the complete picture of the frequency of exoplanets down to  $0.1M_{\oplus}$  that a space-based microlensing survey would provide. Such a survey would probably not detect the planetary host stars for most of the events, and so it cannot provide the systematic data on the variation of exoplanet properties as a function of host star type that a space-based survey will provide.

A space-based microlensing survey, such as MPF, will provide a census of extrasolar planets that is complete (in a statistical sense) down to  $0.1M_{\oplus}$  at orbital separations  $\geq 0.5$  AU, and when combined with the results of the Kepler mission a space-based microlensing survey will give a comprehensive picture of all types of extrasolar planets with masses down to well below an Earth mass. This complete coverage of planets at all separations can be used to calibrate the poorly understood theory of planetary migration. This fundamental exoplanet census data is needed to gain a comprehensive understanding of processes of planet formation and migration, and this understanding of planet formation is an important ingredient for the understanding of the requirements for habitable planets and the development of life on extrasolar planets (Bennett et al., 2007b).

The basic requirements for a space-based microlensing survey are a 1-m class wide field-of-view space telescope that can image the central Galactic bulge in the near-IR or optical almost continuously for periods of at least several months at a time. This can be accomplished as a NASA Discovery mission, as the example of the MPF mission shows, but it could also be combined with other programs that require an IR-optimized wide-FOV space telescope, as long as a large fraction of the observing time is devoted to Galactic bulge observations. As Fig. 1.9 shows, there is no other planned mission that can duplicate the science return of a space-

based microlensing survey, and our knowledge of exoplanets and their formation will remain incomplete until such a mission is flown.

Thus, a space-based microlensing survey is likely to be the only way to gain a comprehensive understanding of the nature of planetary systems, which is needed to understand planet formation and habitability. The proposed Microlensing Planet Finder (MPF) mission is an example of a space-based microlensing survey that can accomplish these objectives with proven technology and a cost that fits comfortably under the NASA Discovery Program cost cap.

## References

- Abe, F., et al. 2004, Search for Low-Mass Exoplanets by Gravitational Microlensing at High Magnification, *Science*, **305**, 1264
- Albrow, M., et al. 1998, The 1995 Pilot Campaign of PLANET: Searching for Microlensing Anomalies through Precise, Rapid, Round-the-Clock Monitoring, *Astrophys. J.*, **509**, 687
- Albrow, M. D., et al. 2000a, Detection of Rotation in a Binary Microlens: PLANET Photometry of MACHO 97-BLG-41, *Astrophys. J.*, **534**, 894
- Albrow, M. D., et al. 2000b, Limits on Stellar and Planetary Companions in Microlensing Event OGLE-1998-BUL-14, *Astrophys. J.*, **535**, 176
- Albrow, M. D., et al. 2001, Limits on the Abundance of Galactic Planets From 5 Years of PLANET Observations, *Astrophys. J. Lett.*, **556**, L113
- Alcock, C., et al. 1993, Possible Gravitational Microlensing of a Star in the Large Magellanic Cloud, *Nature*, **365**, 621
- Alcock, A., et al. 1994, Possible Gravitational Microlensing Event, *I.A.U.C.*, **6068**, 1
- Alcock, C., et al. 1995, First Observation of Parallax in a Gravitational Microlensing Event, *Astrophys. J.*, **454**, L125
- Alcock, C., et al. 1996, Real-Time Detection and Multisite Observations of Gravitational Microlensing, *Astrophys. J. Lett.*, **463**, L67
- Alcock, C., et al. 2000a, The MACHO Project: Microlensing Optical Depth toward the Galactic Bulge from Difference Image Analysis, *Astrophys. J.*, **541**, 734; (E) **557**, 1035
- Alcock, C., et al. 2000b, The MACHO Project: Microlensing Results from 5.7 Years of Large Magellanic Cloud Observations, *Astrophys. J.*, **542**, 281
- An, J., et al. 2002, First Microlens Mass Measurement: PLANET Photometry of EROS BLG-2000-5, *Astrophys. J.*, **572**, 521
- Basri, G., Borucki, W. J., & Koch, D. 2005, The Kepler Mission: A wide-field transit search for terrestrial planets, *New Astronomy Rev.*, **49**, 478
- Beaulieu, J.-P., et al. 2006, Discovery of a Cool Planet of 5.5 Earth Masses Through Gravitational Microlensing, *Nature*, **439**, 437
- Benetti, S., Pasquini, L., & West, R. M. 1995, First spectroscopic confirmation of a microlensing event towards the galactic bulge, *Astron. & Astrophys.*, **294**, L37

- Bennett, D. P. 2004, The Detection of Terrestrial Planets via Gravitational Microlensing: Space vs. Ground-based Surveys, *Extrasolar Planets: Today and Tomorrow*, **321**, 59
- Bennett, D. P. 2005, Large Magellanic Cloud Microlensing Optical Depth with Imperfect Event Selection, *Astrophys. J.*, **633**, 906
- Bennett, D.P. & Rhie, S.H. 1996, Detecting Earth-Mass Planets with Gravitational Microlensing, *Astrophys. J.*, **472**, 660
- Bennett, D.P. & Rhie, S. H., 2002, Simulation of a Space-based Microlensing Survey for Terrestrial Extrasolar Planets, *Astrophys. J.*, **574**, 985
- Bennett, D. P., et al. 1997, Planetary Microlensing from the MACHO Project, *Planets Beyond the Solar System and the Next Generation of Space Missions*, **119**, 95
- Bennett, D. P., et al. 1999, Evidence for a Planet Orbiting a Binary Star System from Gravitational Microlensing, *Nature*, **402**, 57
- Bennett, D. P., et al. 2002, Gravitational Microlensing Events Due to Stellar-Mass Black Holes, *Astrophys. J.*, **579**, 639
- Bennett, D. P., et al. 2004, The Microlensing Planet Finder: Completing the Census of Extrasolar Planets in the Milky Way *SPIE*, **5487**, 1453, (astro-ph/0409218)
- Bennett, D. P., Anderson, J., Bond, I.A., Udalski, A., Gould, A. 2006, Identification of the OGLE-2003-BLG-235/MOA-2003-BLG-53 Planetary Host Star *Astrophys. J. Lett.*, **647**, L171
- Bennett, D. P., Anderson, J., & Gaudi, B. S. 2007a, Characterization of Gravitational Microlensing Planetary Host Stars *Astrophys. J.*, **660**, 781
- Bennett, D. P., et al. 2007b, An Extrasolar Planet Census with a Space-based Microlensing Survey *ArXiv e-prints*, **704**, arXiv:0704.0454
- Bessell, M. S. & Brett, J. M. 1988, JHKLM photometry - Standard systems, passbands, and intrinsic colors *P.A.S.P.*, **100**, 1134
- Bolatto, A. D., & Falco, E. E. 1994, The detectability of planetary companions of compact Galactic objects from their effects on microlensed light curves of distant stars, *Astrophys. J.*, **436**, 112
- Bond, I. A., et al. 2001, Real-time difference imaging analysis of MOA Galactic bulge observations during 2000, *M.N.R.A.S.*, **327**, 868
- Bond, I. A., et al. 2002a, Improving the Prospects for Detecting Extrasolar Planets in Gravitational Microlensing in 2002, *M.N.R.A.S.*, **331**, L19
- Bond, I.A., et al. 2002b, Study by MOA of extra-solar planets in gravitational microlensing events of high magnification, *M.N.R.A.S.*, **333**, 71
- Bond, I.A., et al. 2004, OGLE 2003-BLG-235/MOA 2003-BLG-53: A Planetary Microlensing Event, *Astrophys. J. Lett.*, **606**, L155
- Bourassa, R. R., Kantowski, R., & Norton, T. D. 1973, The Spheroidal Gravitational Lens, *Astrophys. J.*, **185**, 747
- Boss, A. P. 2006, Rapid Formation of Super-Earths around M Dwarf Stars, *Astrophys. J. Lett.*, **644**, L79
- Brown, T., Rosing, W. E., Baliber, N., Hidas, M., & Street, R. 2007, Surveys, Temporal Variability, and the Las Cumbres Observatory Global Telescope, *American Astronomical Society Meeting Abstracts*, 210, #66.01

- Butler, R. P., et al. 2006, Catalog of Nearby Exoplanets, *Astrophys. J.*, **646**, 505
- Chang, K., & Refsdal, S. 1979, Flux variations of QSO 0957+561 A, B and image splitting by stars near the light path, *Nature*, **282**, 561
- Chang, K., & Refsdal, S. 1984, Star disturbances in gravitational lens galaxies, *Astron. & Astrophys.*, **132**, 168
- Delplancke, F., Górski, K. M., & Richichi, A. 2001, Resolving gravitational microlensing events with long-baseline optical interferometry. Prospects for the ESO Very Large Telescope Interferometer, *Astron. & Astrophys.*, **375**, 701
- Dominik, M. 1999, The binary gravitational lens and its extreme cases, *Astron. & Astrophys.*, **349**, 108
- Dominik, M. 2006, *M.N.R.A.S.*, Stochastic distributions of lens and source properties for observed galactic microlensing events, **367**, 669
- Dong, S., et al. 2006, Planetary Detection Efficiency of the Magnification 3000 Microlensing Event OGLE-2004-BLG-343, *Astrophys. J.*, **642**, 842
- Dong, S., et al. 2007, First Space-Based Microlens Parallax Measurement: Spitzer Observations of OGLE-2005-SMC-001, *Astrophys. J.*, **664**, 842
- Gaudi, B. S. 1998, Distinguishing Between Binary-Source and Planetary Microlensing Perturbations, *Astrophys. J.*, **506**, 533
- Gaudi, B. S. & Gould, A. 1997, Planet Parameters in Microlensing Events, *Astrophys. J.*, **486**, 85
- Gaudi, B. S., & Han, C. 2004, The Many Possible Interpretations of Microlensing Event OGLE 2002-BLG-055, *Astrophys. J.*, **611**, 528
- Gaudi, B. S., et al. 2002, Microlensing Constraints on the Frequency of Jupiter-Mass Companions: Analysis of 5 Years of PLANET Photometry, *Astrophys. J.*, **566**, 463
- Gaudi, B. S., et al. 2008, Discovery of a Jupiter/Saturn Analog with Gravitational Microlensing, *Science*, **319**, 927
- Gaudi, B. S., Naber, R. M., & Sackett, P. D. 1998, Microlensing by Multiple Planets in High-Magnification Events, *Astrophys. J. Lett.*, **502**, L33
- Gould, A. 1992, Extending the MACHO search to about  $10^6$  solar masses, *Astrophys. J.*, **392**, 442
- Gould, A. 1997, Extreme Microlensing toward the Galactic Bulge, *Astrophys. J.*, **480**, 188
- Gould, A., Bennett, D. P., & Alves, D. R. 2004, The Mass of the MACHO-LMC-5 Lens Star, *Astrophys. J.*, **614**, 404
- Gould, A., & Gaucherel, C. 1997, Stokes's Theorem Applied to Microlensing of Finite Sources *Astrophys. J.*, **477**, 580
- Gould, A., Gaudi, B. S., & Bennett, D. P. 2007, Ground-based Microlensing Surveys, *ArXiv e-prints*, **704**, arXiv:0704.0767
- Gould, A. & Loeb, A. 1992, Discovering planetary systems through gravitational microlenses, *Astrophys. J.*, **396**, 104
- Gould, A., et al. 2006, Microlens OGLE-2005-BLG-169 Implies That Cool Neptune-like Planets Are Common, *Astrophys. J. Lett.*, **644**, L37



- Graff, D. S., & Gaudi, B. S. 2000, Direct Detection of Large Close-in Planets around the Source Stars of Caustic-crossing Microlensing Events *Astrophys. J. Lett.*, **538**, L133
- Griest, K., & Safizadeh, N. 1998, The Use of High-Magnification Microlensing Events in Discovering Extrasolar Planets, *Astrophys. J.*, **500**, 37
- Hamadache, C., et al. 2006, Galactic Bulge Microlensing Optical Depth from EROS-2, *Astron. & Astrophys.*, **454**, 185
- Han, C. & Gould, A. 1995, The Mass Spectrum of MACHOs from Parallax Measurements, *Astrophys. J.*, **447**, 53
- Hearnshaw, J. B., et al. 2005, The MOA 1.8-metre alt-az wide-field survey telescope and the MOA project, *ArXiv Astrophysics e-prints*, arXiv:astro-ph/0509420
- Ida, S., & Lin, D.N.C. 2004, Toward a Deterministic Model of Planetary Formation. II. The Formation and Retention of Gas Giant Planets around Stars with a Range of Metallicities, *Astrophys. J.*, **616**, 567
- Jaroszynski, M., & Paczyński, B. 2002, A Possible Planetary Event OGLE-2002-BLG-055, *Acta Astronomica*, **52**, 361
- Kennedy, G. M., Kenyon, S. J., & Bromley, B. C. 2006, Planet Formation around Low-Mass Stars: The Moving Snow Line and Super-Earths *Astrophys. J. Lett.*, **650**, L139
- Kervella, P., Thévenin, F., Di Folco, E., & Ségransan, D. 2004, The angular sizes of dwarf stars and subgiants. Surface brightness relations calibrated by interferometry, *Astron. & Astrophys.*, **426**, 297
- Lauer, T. R. 1999, The Photometry of Undersampled Point-Spread Functions, *P.A.S.P.*, **111**, 1434
- Laughlin, G., Bodenheimer, P., & Adams, F.C. 2004, The Core Accretion Model Predicts Few Jovian-Mass Planets Orbiting Red Dwarfs, *Astrophys. J. Lett.*, **612**, L73
- Lewis, G. F. 2001, Gravitational microlensing of stars with transiting planets, *Astron. & Astrophys.*, **380**, 292
- Liebes, S. 1964, Gravitational Lenses, *Physical Review*, **133**, 835
- Mao, S. & Paczyński, B. 1991, Gravitational microlensing by double stars and planetary systems, *Astrophys. J. Lett.*, **374**, L37
- Mao, S. 1999, An Ongoing OGLE Parallax Microlensing Event Toward Carina, *Astron. & Astrophys.*, **350**, L19
- Mao, S. et al. 2002, Optical Gravitational Lensing Experiment. OGLE-1999-BUL-32: the Longest Ever Microlensing Event – Evidence for a Stellar Mass Black Hole?, *M.N.R.A.S.*, **329**, 349
- Paczynski, B. 1986, Gravitational microlensing by the galactic halo, *Astrophys. J.*, **304**, 1
- Peale, S. J. 2003, Comparison of a Ground-based Microlensing Search for Planets with a Search from Space, *Astron. J.*, **126**, 1595
- Poindexter, S., Afonso, C., Bennett, D. P., Glicenstein, J.-F., Gould, A., Szymański, M. K., & Udalski, A. 2005, Systematic Analysis of 22 Microlensing Parallax Candidates, *Astrophys. J.*, **633**, 914

- Popowski, P., et al. 2005, Microlensing Optical Depth toward the Galactic Bulge Using Clump Giants from the MACHO Survey, *Astrophys. J.*, **631**, 879
- Pratt, M. R., et al. 1995, Real-time Detection of Gravitational Microlensing, *ArXiv Astrophysics e-prints*, arXiv:astro-ph/9508039
- Refsdal, S. 1964, The gravitational lens effect, *M.N.R.A.S.*, **128**, 295
- Refsdal, S. 1966, On the possibility of determining the distances and masses of stars from the gravitational lens effect, *M.N.R.A.S.*, **134**, 315
- Rhie, S. H. 1997, Infimum Microlensing Amplification of the Maximum Number of Images of n-Point Lens Systems, *Astrophys. J.*, **484**, 63
- Rhie, S. H. 2001, Can A Gravitational Quadruple Lens Produce 17 images?, *ArXiv Astrophysics e-prints*, arXiv:astro-ph/0103463
- Rhie, S. H. 2002, How Cumbersome is a Tenth Order Polynomial?: The Case of Gravitational Triple Lens Equation, *ArXiv Astrophysics e-prints*, arXiv:astro-ph/0202294
- Rhie, S. H., & Bennett, D. P. 1996, Search for Earth Mass Planets and Dark Matter Too, *Nuclear Physics B Proc. Suppl.*, **51**, 86
- Rhie, S. H., Becker, A. C., Bennett, D. P., Fragile, P. C., Johnson, B. R., King, L. J., Peterson, B. A., & Quinn, J. 1999, Observations of the Binary Microlens Event MACHO 98-SMC-1 by the Microlensing Planet Search Collaboration, *Astrophys. J.*, **522**, 1037
- Rhie, S. H. et al. 2000, On Planetary Companions to the MACHO 98-BLG-35 Microlens Star, *Astrophys. J.*, **533**, 378
- Sahu, K. C. 1994, *Nature*, **370**, 275
- Schneider, P., & Weiss, A. 1986, The two-point-mass lens - Detailed investigation of a special asymmetric gravitational lens, *Astron. & Astrophys.*, **164**, 237
- Schneider, P., & Weiss, A. 1987, A gravitational lens origin for AGN-variability? Consequences of micro-lensing *Astron. & Astrophys.*, **171**, 49
- Smith, M. C., Mao, S., & Woźniak, P. 2002, Parallax Microlensing Events in the OGLE II Database Toward the Galactic Bulge, *M.N.R.A.S.*, **332**, 962
- Smith, M. C., Mao, S., & Paczyński, B. 2003, Acceleration and Parallax Effects in Gravitational Microlensing, *M.N.R.A.S.*, **339**, 925
- Sumi, T. et al. 2003, Microlensing Optical Depth toward the Galactic Bulge from Microlensing Observations in Astrophysics Group Observations during 2000 with Difference Image Analysis, *Astrophys. J.*, **591**, 204
- Sumi, T., et al. 2006, Microlensing Optical Depth toward the Galactic Bulge Using Bright Sources from OGLE-II, *Astrophys. J.*, **636**, 240
- Tisserand, P., et al. 2007, Limits on the Macho content of the Galactic Halo from the EROS-2 Survey of the Magellanic Clouds, *Astron. & Astrophys.*, **469**, 387
- Udalski, A., Szymański, M., Kałużny, J., Kubiak, M., Krzmiński, W., Mateo, M., Preston, G. W., & Paczyński, B. 1993, The optical gravitational lensing experiment. Discovery of the first candidate microlensing event in the direction of the Galactic Bulge *Acta Astronomica*, **43**, 289
- Udalski, A., Szymański, M., Kałużny, J., Kubiak, M., Mateo, M., Krzmiński, W., & Paczyński, B. 1994, The Optical Gravitational Lensing Experiment. The Early Warning System: Real Time Microlensing, *Acta Astronomica*, **44**, 227

- Udalski, A. et al. 2005, A Jovian-Mass Planet in Microlensing Event OGLE-2005-BLG-071, *Astrophys. J. Lett.*, **628**, L109
- Udry, S., et al. 2007, The HARPS search for southern extra-solar planets. XI. Super-Earths (5 and 8  $M_{\oplus}$ ) in a 3-planet system, *Astron. & Astrophys.*, **469**, L43
- van Belle, G. T. 1999, Predicting Stellar Angular Sizes, *P.A.S.P.*, **111**, 1515
- Witt, H. J. 1990, *Astron. & Astrophys.*, 236, 311
- Wolszczan, A., & Frail, D. A. 1992, A planetary system around the millisecond pulsar PSR1257 + 12, *Nature*, **355**, 145
- Wu, X. 1994, Gravitational microlensing by the MACHOs of the Large Magellanic Cloud, *Astrophys. J.*, **435**, 66
- Yanagisawa, T., et al. 2000, Wide-Field Camera for Gravitational Microlensing Survey: MOA-Cam2, *Experimental Astronomy*, **10**, 519
- Yoo, J. et al. 2004, OGLE-2003-BLG-262: Finite-Source Effects from a Point-Mass Lens, *Astrophys. J.*, **603**, 139